Yukon

YGS Open File 2025-1

Geochemistry and geochronology of Cambrian and Upper Ordovician mafic igneous rocks along the Dawson fault zone, Yukon

R.N. Cobbett[1,2], L.P. Beranek[2], M. Colpron[1], S.J. Piercey[2], J.L. Crowley[3], J.V. Strauss[4] and J.F. Taylor[5]

[1] Yukon Geological Survey
[2] Memorial University of Newfoundland
[3] Boise State University
[4] Dartmouth College
[5] Indiana University of Pennsylvania

Published under the authority of the Department of Energy, Mines and Resources, Government of Yukon https://yukon.ca/en/department-energy-mines-resources.

Publié avec l'autorisation du Ministères de l'Énergie, des Mines et des Ressources du gouvernement du Yukon, https://yukon.ca/en/department-energy-mines-resources.

This, and other Yukon Geological Survey publications, may be obtained from:

Yukon Geological Survey
102-300 Main Street
Box 2703 (K-102)
Whitehorse, Yukon, Canada Y1A 2C6

email geology@gov.yk.ca

Visit the Yukon Geological Survey website at https://yukon.ca/en/science-and-natural-resources/geology.

In referring to this publication, please use the following citation:

Cobbett, R.N., Beranek, L.P., Colpron, M., Piercey, S.J., Crowley, J.L., Strauss, J.V. and Taylor, J.F., 2025. Geochemistry and geochronology of Cambrian and Upper Ordovician mafic igneous rocks along the Dawson fault zone, Yukon. Yukon Geological Survey, Government of Yukon, Open File 2025-1, 42 p. plus appendices.

Front cover: Mafic volcanic rocks within the Bouvette Formation near Carpenter Creek. View to the north. Photo credit: Rose Cobbett, Yukon Geological Survey.

Yukon

YGS Open File
2025-1

Geochemistry and geochronology of Cambrian and Upper Ordovician mafic igneous rocks along the Dawson fault zone, Yukon

R.N. Cobbett[1,2], L.P. Beranek[2], M. Colpron[1], S.J. Piercey[2], J.L. Crowley[3], J.V. Strauss[4] and J.F. Taylor[5]

[1] Yukon Geological Survey
[2] Memorial University of Newfoundland
[3] Boise State University
[4] Dartmouth College
[5] Indiana University of Pennsylvania

Table of Contents

Abstract

Neoproterozoic to lower Paleozoic basin and platform strata that formed during and after rifting along the western Laurentian margin are preserved in the northern Cordillera. Several pulses of magmatism occur within margin strata and are concentrated along the Dawson fault in central Yukon. Magmatism is dated as late Cambrian and Late Ordovician using: 1) U-Pb zircon geochronology of volcaniclastic rocks; and 2) fossil ages from strata interbedded with, and enclosing, volcanic rocks. Volcanic rocks from both pulses are predominantly alkaline and basic and erupted in subaqueous environments. The trace element geochemical compositions of the rocks suggest that they formed from partial melting of enriched lithosphere from the garnet stability field.

Plain Language Summary

The ancient western edge of North America partially formed when supercontinent Rodinia broke apart between 700 and 500 million years ago (Ma). The process of continental breakup is associated with small-volume volcanic eruptions that occur under the ocean along the edge of continents. This study investigates the timing of continental breakup-related eruptions that are preserved in central Yukon in an east-west trending belt adjacent to the Dawson fault. Zircon crystals grow in lava as it cools, trapping small amounts of uranium (U). Over millions of years uranium decays to lead (Pb) at a known rate known as half life. Using a mass spectrometer, the uranium and lead within a single zircon grain can be measured and converted to an age of crystallization using half lives, which is the time when lava cooled to form a rock. Using this technique, the ages of eruptions of volcanic rocks along the Dawson fault are precisely calculated as 501–497 Ma, 453 Ma and 445 Ma. Geochemical compositions of these volcanic rocks were determined and compared to similar rocks that form in known tectonic settings (for example, mid-ocean ridges and subduction zones) providing information about the composition of, and depth to, the mantle (layer of the earth below the crust).

Introduction

Mafic lavas and cogenetic intrusive rocks have been recognized in continental margin successions of western North America for decades (e.g., Green, 1972; Gabrielse et al., 1973; Evans and Clemons, 1988; Evans and Zartman, 1988; Roots, 1988; Abbott, 1997; Lund et al., 2010; Pigage et al., 2012; Pigage et al., 2015; Eyster et al., 2018; Campbell et al., 2019; Madronich, 2019; Cobbett et al., 2023). These mafic rocks are the products of Neoproterozoic to early Paleozoic rift processes that resulted in the generation and subsequent modification of the western Laurentian passive margin system (e.g., Yonkee et al., 2014). Targeted field and laboratory studies have focused on interpreting the mantle source and lithogeochemical signature (Goodfellow et al., 1995), eruption or crystallization age (Leslie, 2009) and tectonic setting of the mafic rocks in the Canadian and United States Cordillera (Lund, 2008). The results of these studies indicate several pulses of magmatism have occurred from the Yukon to southwestern USA including Tonian-Cryogenian (720–635 Ma), late Ediacaran to late Cambrian (570–491 Ma) and Early to Late Ordovician (486–445 Ma). The magmatism from all pulses is predominantly alkaline and basic, and erupted in subaqueous environments.

In north-central Yukon, lower Paleozoic mafic volcanic rocks and associated gabbro units are concentrated along the length of the Dawson fault, an east-west trending structure that cuts across the Yukon from the Alaska border in the west to near the border with the Northwest Territories (NWT) in the east (Figs. 1 and 2). This report describes the bedrock geology of areas where volcanic rocks and gabbro are exposed along the Dawson fault, presents U-Pb zircon data and fossil collections that constrain the age of gabbro and volcanic rocks and their whole-rock and Nd-Hf isotopic compositions (Fig. 2). Basic interpretations of the geochemical and geochronological data are presented here, and more comprehensive synthesis and interpretations are provided in Cobbett et al. (2025).

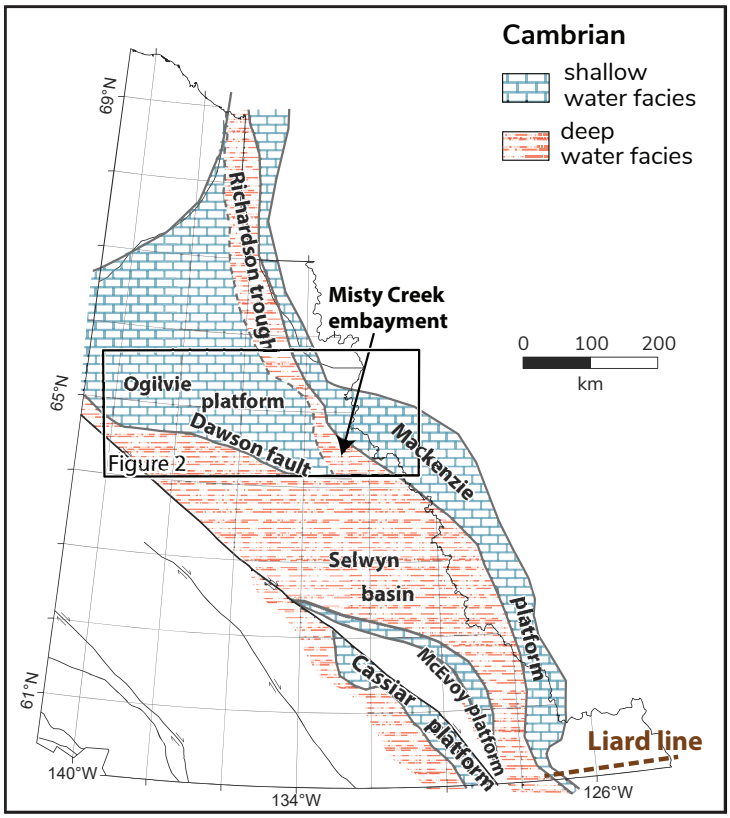

Figure 1. *Map of the Yukon and the western part of the Northwest Territories subdividing the Laurentian margin strata into shallow-water deposits from deep-water deposits. The black box outlines the extent of Figure 2.*

Regional Geology along the Dawson fault

Passive continental margin strata in the northern Cordillera comprise a series of basins and platforms that formed during, and after, continental extension leading to the separation of Laurentia from conjugate blocks (Fig. 1; e.g., Cecile et al., 1997; Li et al., 2008). The Selwyn basin makes up a large portion of the Yukon, east of the Tintina fault, and is one of the largest depo-centres for deep-water deposits in the northern Cordillera (Fig. 1). The Selwyn basin is bounded to the east by the Mackenzie platform and to the north by the Ogilvie platform. The Dawson fault is the boundary between Selwyn basin and Ogilvie platform. It strikes approximately east-west and is mapped as a reverse fault that separates Neoproterozoic to lower Paleozoic basinal rocks to the south from coeval carbonate rocks to the north. Cambrian to Devonian carbonate strata of the Bouvette Formation comprise the footwall (north side) of the Dawson fault for most of its strike length (Figs. 2 and 3). The hanging wall strata include mostly Neoproterozoic to lower Cambrian siliciclastic rocks of the Hyland Group, and locally younger strata (Figs. 2 and 3). Cambrian mafic volcanic rocks and gabbro occur south of the Dawson fault all along its trace and Upper Ordovician mafic volcanic rocks and gabbro sills occur locally north of the fault.

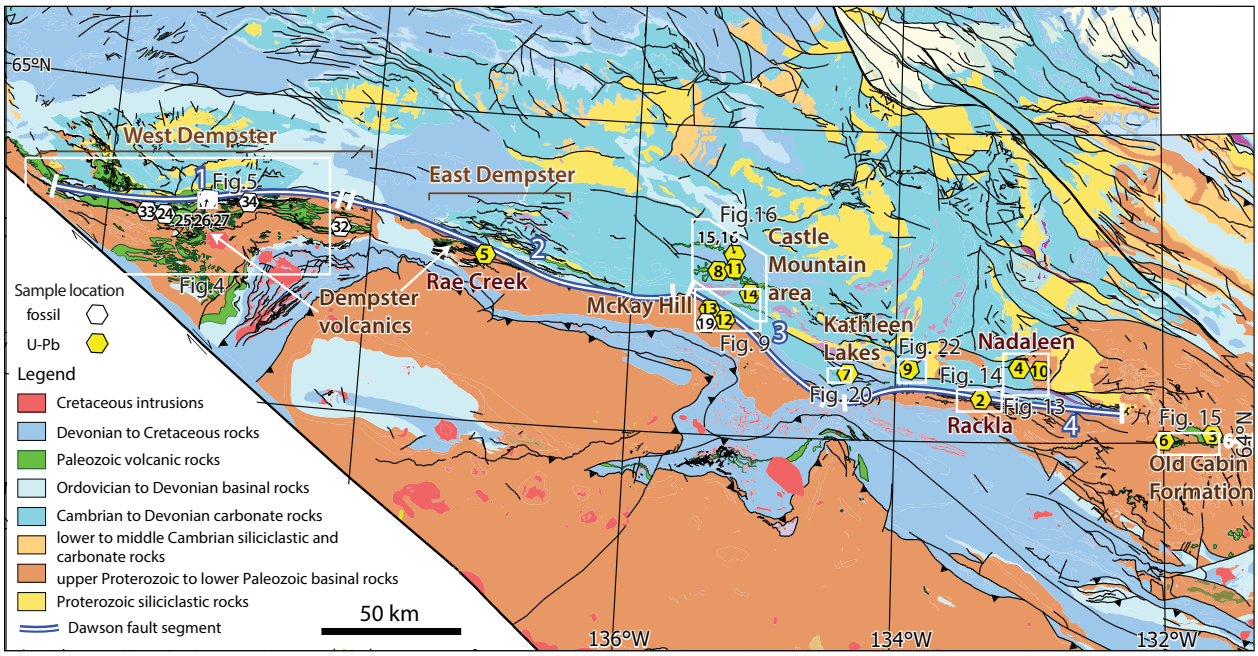

Figure 2. *Simplified regional geology along the Dawson fault corridor. The Dawson fault is divided into four segments based on slightly different strikes of the fault. The U-Pb and fossil geochronological samples that help constrain the age of the volcanic rocks exposed along the Dawson fault corridor are shown in yellow (U-Pb) and white hexagons (fossils) where the numbers correspond to the location column in Table 2. The white boxes outline the extent of Figures 4, 5, 8, 13-16, 21, and 22.*

Data sets

This report presents results from research completed by several geologists over more than a decade. Regional studies by the Yukon Geological Survey (YGS) included 1:50 000 scale bedrock mapping along various segments of the Dawson fault (Colpron, 2012; Colpron et al., 2013; Moynihan, 2014, 2016; MacNaughton et al., 2016; Ambrose and Bowie, 2020; Ambrose, 2021, 2022; Cobbett, 2020, 2022). In addition, targeted studies were focused on igneous rocks exposed in the west Dempster area where systematic sampling of the volcanic rocks

and associated sills were carried out at several locations (Figs. 2 and 4; e.g., Mamrol, 2016). Volcaniclastic rocks and sandstone were sampled for zircon U-Pb geochronology and fossils were collected wherever they were uncovered (Tables 1 and 2).

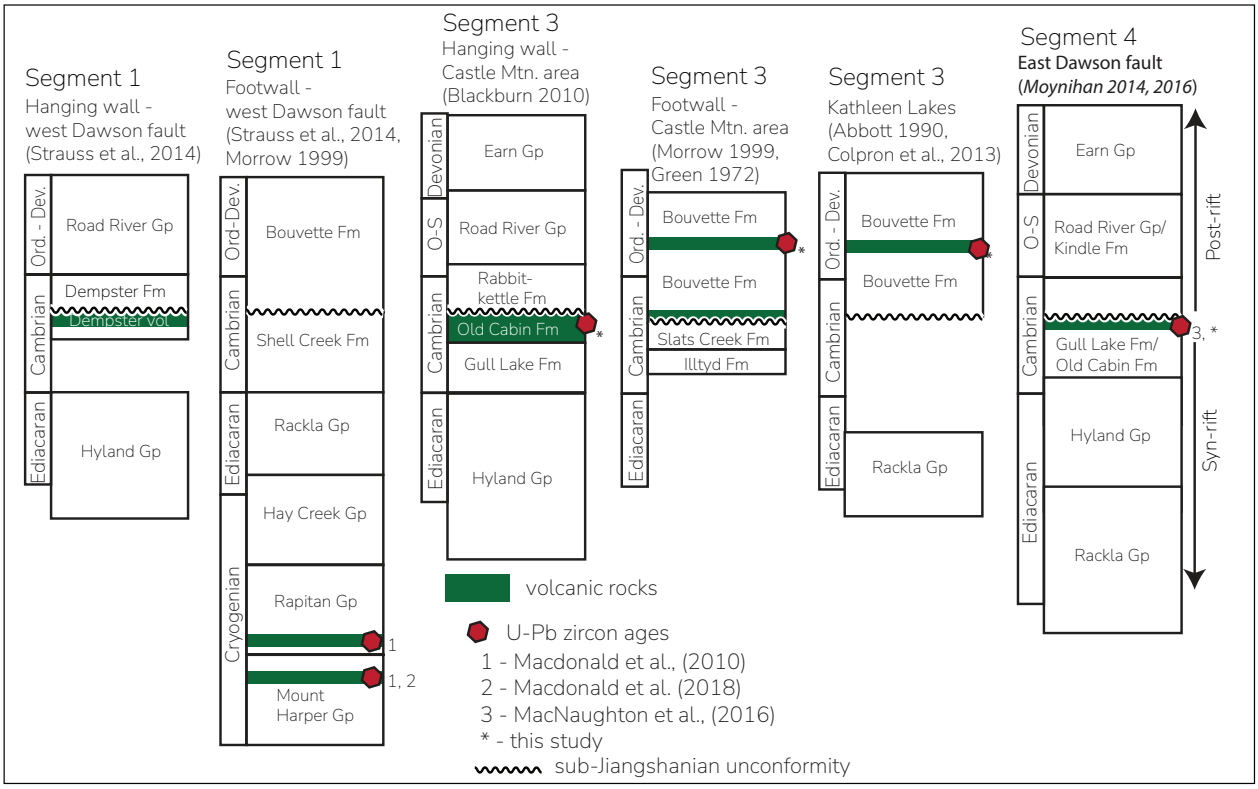

Figure 3. *Simplified regional stratigraphy for the hanging wall and footwall of the Dawson fault that accounts for the changes in geology from its western edge to the eastern edge of the fault. For more detailed stratigraphy for each area, refer to the references provided.*

Analytical methods

U-Pb geochronology

Zircons recovered from sandstone, volcaniclastic sandstone and basalt breccia were analyzed using laser ablation inductively coupled plasma mass spectrometry (LA-ICP-MS; Appendix A, Table A1) and chemical abrasion isotope dilution thermal ionization mass spectrometry (CA-ID-TIMS; Table 1) methods at the Isotope Geology Laboratory, Boise State University. Zircon grains were first imaged by cathodoluminescence (CL) and analyzed by LA-ICP-MS to characterize the zircon populations (Appendix A, Fig. A1). A subset of the zircon grains that comprised the youngest statistically coherent age population with similar chemical composition and morphology were subsequently analyzed by CA-ID-TIMS. Weighted mean $^{206}Pb/^{238}U$ dates were calculated from equivalent CA-ID-TIMS dates (probability of fit (pof) >0.05) using Isoplot 3.0 (Ludwig, 2003). Errors on weighted mean dates are given as ± x / y / z, where x is the internal error based on analytical uncertainties only, including: counting statistics, subtraction of tracer solution, and blank and initial common Pb subtraction; y includes the tracer calibration uncertainty propagated in quadrature; and z includes the ^{238}U decay constant uncertainty propagated in quadrature. Internal errors should be considered when comparing the dates with $^{206}Pb/^{238}U$ dates from other laboratories that used the same tracer solution or a tracer solution that was cross calibrated using EARTHTIME gravimetric standards. Errors including the

uncertainty in the tracer calibration should be considered when comparing the dates with those derived from other geochronological methods using the U-Pb decay scheme (e.g., LA-ICP-MS). Errors including uncertainties in the tracer calibration and ^{238}U decay constant (Jaffey et al., 1971) should be considered when comparing the dates with those derived from other decay schemes (e.g., $^{40}Ar/^{39}Ar$, ^{187}Re-^{187}Os). Errors are reported at the 2σ (95% confidence interval).

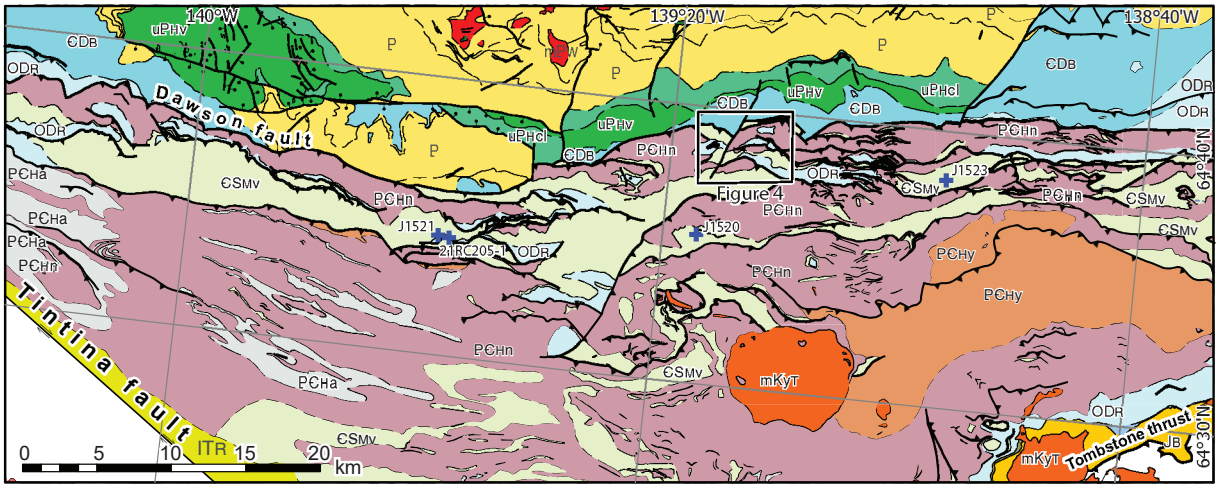

Figure 4. *Bedrock geology map of the Dawson fault segment 1 (Yukon Geological Survey, 2024).*

LA-ICP-MS methods

Zircon grains were separated from rocks using standard techniques, annealed at 900°C for 60 hours in a muffle furnace, and mounted in epoxy and polished until their centres were exposed. Cathodoluminescence images were obtained with a JEOL JSM-300 scanning electron microscope and Gatan MiniCL or a Hitachi TM4000Plus scanning electron microscope. Zircon was analyzed by LA-ICP-MS using two different instruments. Three samples (18PS016, 19RC016-1, 19RC170-1) were analyzed with a ThermoElectron X-Series II quadrupole inductively coupled plasma mass spectrometer (ICP-MS) and New Wave Research UP-213

Nd:YAG UV (213 nm) laser ablation system. In-house analytical protocols, standard materials and data reduction software were used for acquisition and calibration of U-Pb dates and a suite of high field strength elements (HFSE) and rare earth elements (REE). Zircon was ablated with a laser spot of 25 µm wide using fluence and pulse rates of 5 J/cm^2 and 5 Hz, respectively, during a 45 second analysis (15 second gas blank, 30 second ablation) that excavated a pit ~15 µm deep. Ablated material was carried by a 1.2 L/min He gas stream to the nebulizer flow of the plasma. Dwell times are given in instrumental data in Appendix A, Table A1. Ten samples (11MC059, 12MC162-2, 19TA095, JB-1901, 20RC-043, 20RC092-1, 20RC142-1, 20RC173-2, 22RC029-1, 22RC029-2) were analyzed with an iCAP RQ Quadrupole ICP-MS and Teledyne Photon Machines Analyte Excite+ 193 nm excimer laser ablation system with HelEx II Active two-volume ablation cell. In-house analytical protocols, standard materials and data reduction software were used for acquisition and calibration of U-Pb dates and a suite of HFSE and REE. Zircon was ablated with a laser spot of 20 µm wide using fluence and pulse rates of 3 J/cm^2 and 10 Hz, respectively, during a 35 second analysis (15 second gas blank, 20 second ablation) that excavated a pit ~8 µm deep. Ablated material was carried by a 0.5 L/min He gas stream in the inner cell and a 1.1 L/min He gas stream in the outer cell. Dwell times are given in instrumental data in Appendix A, Table A1.

Background count rates for each analyte were obtained prior to each spot analysis and subtracted from the raw count rate for each analyte. Ablation pits that appear to have intersected glass or mineral inclusions were identified based on Ti and P. The U-Pb dates from these analyses are considered valid if the U-Pb ratios appear to have been unaffected by the inclusions. Analyses that appear contaminated by common Pb were rejected based on mass 204 being above baseline. For concentration calculations, background subtracted count rates for each analyte were internally normalized to ^{29}Si and calibrated with respect to NIST SRM-610 and -612 glasses as the primary standards. Temperature was calculated from the Ti-in-zircon thermometer (Watson et.al., 2006). Because there are no constraints on the activity of TiO_2, an average value in crustal rocks of 0.8% was used.

For U-Pb and ^{207}Pb/^{206}Pb dates, instrumental fractionation of the background subtracted ratios was corrected and dates were calibrated with respect to interspersed measurements of zircon standards and reference materials. The primary standard Plešovice zircon (Sláma et al., 2008) was used to monitor time dependent instrumental fractionation based on two analyses for every 10 analyses of unknown zircon. A secondary correction to the ^{206}Pb/^{238}U dates was made based on results from the zircon standards of Seiland (531 Ma; Kuiper et al., 2022), Zirconia (327 Ma; Boise State University, pers. comm.) and 91500 (Wiedenbeck et al., 1995), which were treated as unknowns and measured once for every 10 to 12 analyses of unknown zircon. These results showed a linear age bias of several percent that is related to the ^{206}Pb count rate. The secondary correction is thought to mitigate matrix-dependent variations due to contrasting compositions and ablation characteristics between the Plešovice zircon and other standards (and unknowns).

Radiogenic isotope ratio and age error propagation for all analyses includes uncertainty contributions from counting statistics and background subtraction. The standard calibration uncertainty for U-Pb is the local standard deviation of the polynomial fit to the fractionation factor of Plešovice versus time and for ^{207}Pb/^{206}Pb is the standard error of the mean of the fractionation factor of Plešovice. These uncertainties are given in instrumental data in Appendix A, Table A1. Errors without the standard calibration uncertainty are given below. Age interpretations are based on ^{206}Pb/^{238}U dates. Errors are at 2σ.

Table 1. *Chemical abrasion isotope dilution thermal ionization mass spectrometry data table.*

									Radiogenic isotope ratios									Isotopic dates								
Sample	LA-ICPMS spot label	Th U	^{206}Pb* x10^{-13} mol	mol % ^{206}Pb*	Pb* (pg)	Pb$_c$ (pg)	Pb* Pb$_c$	^{206}Pb ^{204}Pb	^{208}Pb ^{206}Pb	^{207}Pb ^{206}Pb	% err	^{207}Pb ^{235}U	% err	^{206}Pb ^{238}U	% err	corr. coef.	include in weighted mean?	^{207}Pb ^{206}Pb	±	^{207}Pb ^{235}U	±	^{206}Pb ^{238}U	±	***Weighted mean calculations 2 σ errors***		
(a)		(b)	(c)	(c)	(c)	(c)	(c)	(d)	(e)	(e)	(f)	(e)	(f)	(e)	(f)			(g)	(f)	(g)	(f)	(g)	(f)			
11MC059 - Lat: 64.1470; Long: -133.3842; Location 2																										
z4	none	2.639	1.5071	99.73%	58.7	0.34	172	6629	0.8258	0.057141	0.100	0.635407	0.160	0.080685	0.073	0.8925		496.00	2.21	499.46	0.63	500.21	0.35		206Pb/238U ± random (+tracer) [+decay constant]	MSWD =	0.6
z1	none	2.070	1.0114	99.57%	35.7	0.36	99	4239	0.6477	0.057162	0.131	0.634834	0.192	0.080584	0.089	0.8118		496.79	2.88	499.10	0.76	499.61	0.43	x	**499.42 ± 0.24** (0.28) [0.59]	pof =	0.56
z2	354	2.382	0.6740	99.43%	25.1	0.32	78	3150	0.7451	0.057286	0.192	0.635856	0.244	0.080539	0.082	0.7361		501.56	4.23	499.74	0.96	499.34	0.40	x		n =	3
z5	399	2.594	0.5182	99.22%	20.0	0.34	60	2324	0.8116	0.057258	0.223	0.635514	0.276	0.080534	0.091	0.6954		500.51	4.91	499.52	1.09	499.31	0.44	x			
z3	none	2.483	0.6178	99.40%	23.4	0.31	76	2998	0.7770	0.057157	0.168	0.630228	0.221	0.080006	0.077	0.7796		496.60	3.70	496.24	0.87	496.16	0.37				
12MC162-2 - Lat: 64.2454, Long: -133.0676; Location 4																										
z1	45	5.618	2.0670	99.88%	120.5	0.20	604	15530	1.7562	0.057624	0.084	0.661541	0.142	0.083300	0.072	0.8970		514.51	1.84	515.56	0.57	515.79	0.36		206Pb/238U ± random (+tracer) [+decay constant]	MSWD =	0.5
z4	108	0.688	1.4037	99.67%	36.9	0.38	97	5534	0.2152	0.057503	0.112	0.647159	0.166	0.081661	0.072	0.8475		509.88	2.46	506.73	0.66	506.03	0.35		**499.82 ± 0.19** (0.24) [0.59]	pof =	0.71
z3	103	0.374	0.8479	99.72%	20.5	0.20	103	6399	0.1169	0.057385	0.105	0.641518	0.161	0.081116	0.071	0.8765		505.37	2.30	503.25	0.64	502.78	0.34			n =	4
z7	115	0.794	0.4273	98.58%	11.5	0.51	22	1266	0.2484	0.057131	0.330	0.634955	0.380	0.080643	0.093	0.6251		495.60	7.27	499.18	1.50	499.96	0.45	x			
z6	112	0.638	0.2594	98.90%	6.7	0.24	28	1637	0.1997	0.057183	0.274	0.635426	0.326	0.080629	0.085	0.6890		497.62	6.04	499.47	1.28	499.87	0.41	x			
z2	52	0.582	1.9881	99.85%	50.8	0.26	199	11646	0.1821	0.057330	0.079	0.637052	0.140	0.080628	0.071	0.9252		503.27	1.73	500.48	0.55	499.87	0.34	x			
z5	109	0.555	3.2682	99.88%	83.0	0.32	261	15422	0.1737	0.057226	0.068	0.635630	0.132	0.080594	0.069	0.9655		499.28	1.49	499.60	0.52	499.67	0.33	x			
15MC024 - Lat: 64.5422, Long: -137.1625; Location 5																										
z11	2	1.097	0.0961	98.26%	2.8	0.14	20	1035	0.343	0.057773	0.493	0.663051	0.557	0.083276	0.113	0.637		520.17	10.82	516.48	2.26	515.65	0.56	x	207Pb/206Pb ± random [+decay constant]	MSWD =	0.7
z10	3	1.096	0.1104	98.52%	3.2	0.14	23	1219	0.343	0.057748	0.448	0.652728	0.507	0.082015	0.103	0.638		519.21	9.84	510.16	2.03	508.14	0.50	x	**514.11 ± 2.17** [3.32]	pof =	0.66
z9	6	1.126	0.0435	96.41%	1.3	0.13	9	503	0.352	0.057712	1.110	0.644116	1.200	0.080982	0.187	0.544		517.86	24.36	504.85	4.78	501.98	0.91	x		n =	9
z5	none	1.365	0.4277	99.32%	13.1	0.24	54	2668	0.427	0.057676	0.190	0.650865	0.245	0.081882	0.072	0.828		516.50	4.18	509.01	0.98	507.34	0.35	x			
z8	5	1.370	0.1540	96.88%	4.7	0.41	11	578	0.428	0.057656	0.641	0.660250	0.716	0.083092	0.161	0.552		515.73	14.07	514.77	2.89	514.55	0.80	x			
z4	none	1.862	0.0779	94.60%	2.6	0.37	7	334	0.582	0.057642	1.369	0.660150	1.465	0.083099	0.141	0.706		515.21	30.06	514.71	5.91	514.59	0.70	x			
z2	none	2.230	0.2785	98.92%	10.1	0.25	40	1670	0.697	0.057580	0.294	0.650466	0.344	0.081969	0.079	0.693		512.83	6.47	508.77	1.37	507.86	0.39	x			
z3	none	1.020	0.5889	99.40%	16.7	0.30	57	2998	0.319	0.057557	0.154	0.640595	0.207	0.080757	0.075	0.795		511.96	3.39	502.67	0.82	500.64	0.36	x			
z1	none	1.044	0.3233	99.04%	9.2	0.26	36	1883	0.327	0.057555	0.346	0.650064	0.397	0.081953	0.079	0.699		511.88	7.61	508.52	1.59	507.77	0.39	x			
19TA095 - Lat: 64.2296, Long: -133.8861; Location 9																										
z8	23,24	0.664	0.7325	99.82%	19.1	0.11	170	9759	0.208	0.056157	0.094	0.564652	0.155	0.072957	0.072	0.921		457.59	2.07	454.55	0.57	453.95	0.32		^{206}Pb/^{238}U ± random (+tracer) [+decay constant]	MSWD =	2.1
z3	5,6	0.721	5.5894	99.94%	147.9	0.27	540	30551	0.226	0.056069	0.064	0.563412	0.128	0.072912	0.069	0.966		454.11	1.43	453.75	0.47	453.67	0.30		**453.04 ± 0.15** (0.27) [0.54]	pof =	0.09
z2	3,4	0.845	6.4780	99.97%	176.6	0.17	1027	56396	0.265	0.056032	0.063	0.563010	0.127	0.072907	0.068	0.971		452.65	1.39	453.48	0.46	453.65	0.30			n =	4
z5	15,16	0.732	0.8378	99.77%	22.2	0.16	139	7885	0.230	0.056020	0.102	0.562426	0.158	0.072847	0.070	0.881		452.17	2.26	453.10	0.58	453.29	0.31	x			
z6	17,18	0.992	6.2242	99.97%	175.7	0.17	1046	55485	0.311	0.056094	0.064	0.563023	0.127	0.072828	0.069	0.966		455.11	1.41	453.49	0.47	453.17	0.30	x			
z7	21,22	0.351	0.5239	99.75%	12.6	0.11	115	7206	0.110	0.056028	0.175	0.561987	0.221	0.072780	0.074	0.724		452.50	3.89	452.82	0.81	452.88	0.33	x			
z1	1,2	0.414	2.2500	99.91%	55.0	0.16	337	20652	0.130	0.056019	0.072	0.561815	0.134	0.072769	0.069	0.950		452.14	1.59	452.71	0.49	452.82	0.30	x			
z4	9,10	0.925	5.0020	99.96%	139.0	0.16	843	45450	0.290	0.056064	0.064	0.561067	0.128	0.072615	0.069	0.968		453.89	1.41	452.22	0.47	451.89	0.30				
JB-1901-A - Lat: 64.234, Long: -132.953; Location 10																										
z5	none	0.736	6.4005	99.77%	170.1	1.21	141	8041	0.230	0.057330	0.070	0.641523	0.134	0.081194	0.069	0.960		503.27	1.53	503.25	0.53	503.24	0.34		^{206}Pb/^{238}U ± random (+tracer) [+decay constant]	MSWD =	0.2
z6	none	0.596	5.5467	99.97%	142.3	0.15	959	56006	0.186	0.057371	0.073	0.640413	0.132	0.080996	0.069	0.924		504.82	1.61	502.56	0.52	502.07	0.33	x	**501.98 ± 0.17** (0.29) [0.60]	pof =	0.90
z1	none	0.512	4.6241	99.96%	116.1	0.15	788	47017	0.160	0.057338	0.064	0.639961	0.128	0.080985	0.069	0.964		503.56	1.42	502.28	0.51	502.00	0.33	x		n =	4
z2	none	0.536	3.7969	99.94%	96.0	0.18	533	31616	0.168	0.057381	0.067	0.640343	0.130	0.080973	0.070	0.958		505.21	1.47	502.52	0.52	501.93	0.34	x			
z3	none	0.523	14.5310	99.98%	366.0	0.26	1385	82359	0.163	0.057355	0.063	0.640026	0.127	0.080969	0.070	0.959		504.23	1.39	502.32	0.50	501.90	0.34	x			
19RC170-1 - Lat: 64.5287, Long: -135.3211; Location 8																										
z1	167	1.002	7.6951	99.96%	217.7	0.27	821	43470	0.314	0.055874	0.063	0.551564	0.127	0.071627	0.069	0.968		446.38	1.39	446.02	0.46	445.95	0.30	x	^{206}Pb/^{238}U ± random (+tracer) [+decay constant]	MSWD =	1.5
z3	169	0.979	5.9668	99.84%	167.9	0.81	207	11032	0.307	0.055929	0.068	0.551753	0.132	0.071582	0.069	0.964		448.54	1.50	446.14	0.48	445.68	0.30	x	**445.64 ± 0.12** (0.25) [0.53]	pof =	0.17
z2	168	0.680	2.8257	99.92%	74.0	0.19	389	22276	0.213	0.055921	0.070	0.551672	0.133	0.071581	0.071	0.950		448.25	1.55	446.09	0.48	445.67	0.30	x		n =	6
z5	177	0.816	6.5418	99.96%	177.2	0.23	786	43453	0.256	0.055925	0.063	0.551619	0.128	0.071569	0.070	0.966		448.41	1.39	446.06	0.46	445.60	0.30	x			
z6	175	0.999	8.9854	99.98%	254.1	0.15	1654	87584	0.314	0.055957	0.063	0.551883	0.127	0.071563	0.070	0.963		449.65	1.39	446.23	0.46	445.57	0.30	x			
z4	173	0.627	2.2356	99.92%	57.8	0.15	374	21701	0.197	0.055894	0.073	0.551037	0.134	0.071533	0.069	0.941		447.17	1.62	445.68	0.48	445.39	0.30	x			
20RC043 - Lat: 64.5350, Long: -135. 2470; Location 11																										
z5	535	0.574	1.5852	99.84%	40.4	0.21	196	11503	0.180	0.056138	0.079	0.564036	0.141	0.072903	0.070	0.934		456.82	1.76	454.15	0.52	453.62	0.31	x	^{206}Pb/^{238}U ± random (+tracer) [+decay constant]	MSWD =	0.8
z1	537	0.585	1.5658	99.85%	40.0	0.19	212	12421	0.184	0.056079	0.078	0.563259	0.140	0.072878	0.070	0.940		454.52	1.73	453.65	0.51	453.47	0.31	x	**453.42 ± 0.14** (0.19) [0.51]	pof =	0.52
z2	532	0.538	0.6720	99.57%	17.0	0.24	70	4180	0.169	0.056195	0.132	0.564319	0.186	0.072865	0.072	0.838		459.09	2.93	454.33	0.68	453.39	0.32	x		n =	5
z6	533	0.501	1.3020	99.61%	32.6	0.43	76	4575	0.157	0.056130	0.110	0.563610	0.165	0.072858	0.071	0.864		456.52	2.44	453.87	0.60	453.35	0.31	x			
z4	536	0.608	1.9342	99.85%	49.8	0.25	201	11712	0.191	0.056113	0.077	0.563322	0.138	0.072843	0.069	0.940		455.86	1.70	453.69	0.50	453.26	0.30	x			
20RC173-2 - Lat: 64.4631, Long: -135.0888; Location 14																										
z5	867	0.969	7.7105	99.98%	216.6	0.14	1516	80819	0.303	0.057421	0.063	0.647722	0.127	0.081848	0.069	0.964		506.76	1.39	507.08	0.51	507.15	0.34				
z6	888	1.223	9.3647	99.98%	278.5	0.13	2145	108005	0.382	0.057431	0.059	0.647541	0.125	0.081811	0.070	0.978		507.15	1.30	506.96	0.50	506.92	0.34				
z3	869	0.640	3.1110	99.88%	80.7	0.32	252	14574	0.200	0.057428	0.067	0.645939	0.133	0.081614	0.070	0.965		507.02	1.48	505.98	0.53	505.75	0.34				
z1	758	0.971	11.1997	99.99%	314.7	0.12	2565	136694	0.304	0.057204	0.061	0.636725	0.125	0.080765	0.069	0.972		498.40	1.34	500.28	0.50	500.69	0.33				
z4b	904	1.127	5.5408	99.96%	161.3	0.20	814	41901	0.353	0.057284	0.039	0.635500	0.089	0.080496	0.054	0.966		501.51	0.87	499.52	0.35	499.08	0.26				
z2	884	0.952	4.6815	99.97%	131.0	0.10	1255	67213	0.298	0.057132	0.062	0.629812	0.127	0.079988	0.069	0.972		495.63	1.38	495.98	0.50	496.05	0.33				
z4a	904	1.196	14.4300	99.98%	426.7	0.27	1600	81061	0.374	0.057113	0.041	0.616982	0.089	0.078385	0.054	0.948		494.90	0.91	487.95	0.34	486.48	0.25				
20RC092-1 - Lat: 64.3597, Long: -135.3502; Location 12																										
z1	615	14.998	0.0616	96.47%	7.3	0.19	39	512	4.693	0.057276	0.959	0.633416	1.040	0.080243	0.146	0.601		501.19	21.11	498.22	4.09	497.57	0.70				
20RC142-1 - Lat: 64.3891, Long: -135.4244; Location 13																										
z2	646	1.670	7.5387	99.97%	246.2	0.20	1227	56270	0.523	0.057349	0.064	0.635857	0.128	0.080450	0.070	0.960		503.99	1.41	499.74	0.51	498.81	0.34	x	^{206}Pb/^{238}U ± random (+tracer) [+decay constant]	MSWD =	1.3
z1	651	2.433	7.8533	99.97%	295.4	0.21	1406	55990	0.761	0.057259	0.062	0.634643	0.127	0.080423	0.070	0.966		500.53	1.37	498.98	0.50	498.65	0.34	x	**498.54 ± 0.15** (0.21) [0.56]	pof =	0.30
z5	652	2.096	5.8002	99.96%	205.4	0.19	1068	45180	0.656	0.057286	0.063	0.634701	0.127	0.080392	0.069	0.968		501.58	1.39	499.02	0.50	498.46	0.33	x		n =	5
z3	679	3.107	3.2723	99.88%	137.4	0.34	410	14619	0.972	0.057269	0.081	0.634466	0.138	0.080387	0.070	0.907		500.90	1.78	498.87	0.55	498.43	0.33	x			
z4	659	3.566	2.1121	99.91%	95.0	0.16	597	19885	1.116	0.057243	0.074	0.634064	0.136	0.080371	0.070	0.938		499.93	1.63	498.62	0.54	498.34	0.34	x			
19RC016-1 - Lat: 64. 2149, Long: -134.4552; Location 7																										
z6	84	0.667	2.8955	99.90%	75.6	0.24	320	18393	0.209	0.055921	0.090	0.552960	0.144	0.071749	0.071	0.866		448.23	1.99	446.93	0.52	446.68	0.31	x	^{206}Pb/^{238}U ± random (+tracer) [+decay constant]	MSWD =	2.1
z4	81	0.854	10.8832	99.98%	297.4	0.17	1752	96045	0.268	0.055852	0.061	0.552268	0.126	0.071748	0.069	0.970		445.47	1.36	446.48	0.45	446.68	0.30	x	**446.45 ± 0.13** (0.25) [0.53]	pof =	0.08
z3	67	0.900	14.3695	99.99%	397.0	0.17	2364	128150	0.282	0.055854	0.061	0.551920	0.125	0.071700	0.069	0.971		445.56	1.35	446.25	0.45	446.39	0.30	x		n =	5
z2	85	0.606	1.3749	99.85%	35.3	0.17	212	12342	0.190	0.055854	0.082	0.551772	0.142	0.071680	0.070	0.929		445.59	1.82	446.16	0.51	446.27	0.30	x			
z1	83	1.337	13.8879	99.99%	423.3	0.17	2505	123074	0.419	0.055853	0.060	0.551713	0.125	0.071674	0.069	0.975		445.53	1.33	446.12	0.45	446.23	0.30	x			
z5	76	0.840	15.6113	99.98%	425.2	0.23	1855	102026	0.264	0.055835	0.061	0.550001	0.126	0.071475	0.070	0.967		444.80	1.36	445.00	0.45	445.04	0.30				
18PS016-1 - Lat: 63.9988, Long: -131.9521; Location 6																										
z1	74-75	5.942	0.5213	99.46%	31.5	0.24	134	3332	1.859	0.057309	0.164	0.637829	0.222	0.080719	0.095	0.748		503.46	3.61	500.96	0.88	500.41	0.46	x	^{206}Pb/^{238}U ± random (+tracer) [+decay constant]	MSWD =	1.4
z2	72-73	3.740	0.5501	99.43%	25.4	0.26	97	3152	1.170	0.057189	0.160	0.636495	0.217	0.080721	0.091	0.754		498.81	3.53	500.13	0.86	500.42	0.44	x	**500.22 ± 0.25** (0.34) [0.62]	pof =	0.24
z4	79-80	2.272	0.4377	99.41%	16.0	0.22	74	3040	0.711	0.057125	0.181	0.635137	0.233	0.080639	0.082	0.746		496.35	3.98	499.29	0.92	499.93	0.40	x		n =	4
z6	85	26.349	0.0881	97.35%	17.0	0.20	86	682	8.244	0.056955	0.979	0.632793	1.111	0.080580	0.368	0.503		489.80	21.60	497.83	4.37	499.58	1.77	x			
22RC029-1 - Lat: 64.5657, Long: -135. 2669; Location 15																										
z5	70	0.605	3.4322	99.95%	88.2	0.14	648	37749	0.190	0.055985	0.065	0.554645	0.130	0.071884	0.070	0.961		450.79	1.45	448.03	0.47	447.50	0.30		^{206}Pb/^{238}U ± random (+tracer) [+decay constant]	MSWD =	1.0
z3	25	0.836	2.4753	99.94%	67.4	0.12	547	30109	0.262	0.055916	0.067	0.553769	0.131	0.071860	0.070	0.959		448.02	1.49	447.46	0.47	447.35	0.30		**446.66 ± 0.24** (0.27) [0.52]	pof =	0.40
z6	43	0.694	3.7276	99.95%	98.0	0.17	590	33618	0.218	0.055871	0.067	0.552613	0.130	0.071768	0.069	0.957		446.23	1.49	446.71	0.47	446.80	0.30	x		n =	4
z1	31	0.651	3.8010	99.95%	98.8	0.15	650	37453	0.204	0.055878	0.067	0.552580	0.131	0.071755	0.069	0.963		446.51	1.50	446.69	0.47	446.72	0.30	x			
z2	30	0.950	7.0494	99.98%	197.1	0.13	1522	81524	0.298	0.055885	0.062	0.552559	0.127	0.071743	0.069	0.968		446.80	1.38	446.67	0.46	446.65	0.30	x			
z4	16	0.879	3.3461	99.95%	92.0	0.13	702	38283	0.276	0.055832	0.074	0.551782	0.134	0.071710	0.071	0.926		444.69	1.64	446.16	0.48	446.45	0.31	x			
22RC029-2 - Lat: 64.5657, Long: -135.2669; Location 16																										
z3	76	0.698	3.5960	99.93%	94.6	0.22	422	24062	0.219	0.055897	0.068	0.552215	0.133	0.071683	0.072	0.952		447.27	1.52	446.45	0.48	446.29	0.31	x	^{206}Pb/^{238}U ± random (+tracer) [+decay constant]	MSWD =	0.9
z5	79	0.763	4.6645	99.95%	124.7	0.21	594	33307	0.239	0.055860	0.067	0.551841	0.131	0.071681	0.070	0.960		445.82	1.48	446.20	0.47	446.28	0.30	x	**446.14 ± 0.13** (0.18) [0.51]	pof =	0.51
z4	78	0.831	1.6120	99.74%	43.8	0.34	127	7024	0.261	0.055884	0.092	0.551965	0.151	0.071667	0.071	0.901		446.77	2.05	446.28	0.54	446.19	0.31	x		n =	6
z1	82	0.924	1.2483	99.53%	34.7	0.49	70	3812	0.290	0.055885	0.122	0.551873	0.175	0.071654	0.071	0.839		446.79	2.71	446.22	0.63	446.11	0.31	x			
z2	88	0.703	0.9072	99.84%	23.9	0.12	194	11040	0.220	0.055880	0.095	0.551688	0.158	0.071636	0.082	0.878		446.59	2.10	446.10	0.57	446.01	0.35	x			
z6	80	0.781	2.7313	99.91%	73.3	0.21	349	19481	0.245	0.055863	0.069	0.551436	0.132	0.071624	0.069	0.957		445.94	1.54	445.94	0.48	445.94	0.30	x			

(a) z1, z2, etc. are labels for analyses composed of single zircon grains that were annealed and chemically abraded (Mattinson, 2005).
(b) Model Th/U ratio calculated from radiogenic ^{208}Pb/^{206}Pb ratio and ^{207}Pb/^{235}U date.
(c) Pb* and Pbc are radiogenic and common Pb, respectively. mol % ^{206}Pb* is with respect to radiogenic and blank Pb.
(d) Measured ratio corrected for spike and fractionation only. Pb fractionation correction for analyses done with tracer solution BSU1B is 0.16 ± 0.03 (1 sigma) or 0.18 ± 0.03 (1 sigma) %/amu (atomic mass unit) for single-collector Daly analyses, based on recent analyses of EARTHTIME ^{202}Pb-^{205}Pb ET2535 tracer solution.
(e) Corrected for fractionation and spike. Common Pb in zircon analyses is assigned to procedural blank with composition of ^{206}Pb/^{204}Pb = 18.04 ± 0.61%; ^{207}Pb/^{204}Pb = 15.54 ± 0.52%; ^{208}Pb/^{204}Pb = 37.69 ± 0.63% (1 sigma).
^{206}Pb/^{238}U and ^{207}Pb/^{206}Pb ratios corrected for initial disequilibrium in ^{230}Th/^{238}U using a D(Th/U) of 0.20 ± 0.05 (1 sigma).
(f) Errors are 2 sigma, propagated using algorithms of Schmitz and Schoene (2007) and Crowley et al. (2007).
(g) Calculations based on the decay constants of Jaffey et al. (1971). ^{206}Pb/^{238}U and ^{207}Pb/^{206}Pb dates corrected for initial disequilibrium in ^{230}Th/^{238}U using a D(Th/U) of 0.20 ± 0.05 (1 sigma).

CA-ID-TIMS methods

The U-Pb dates were obtained by the chemical abrasion isotope dilution thermal ionization mass spectrometry (CA-ID-TIMS) method from analyses composed of single zircon grains (Table 1), modified after Mattinson (2005). Zircon was removed from the epoxy mounts for dating based on CL images and LA-ICP-MS data.

Zircon was put into 3 ml Teflon PFA beakers and loaded into 300 µl Teflon PFA microcapsules. Fifteen microcapsules were placed in a large capacity Parr vessel and the zircon partially dissolved in 120 µl of 29 M HF for 12 hours at 190°C. Zircon was returned to 3 ml Teflon PFA beakers, HF was removed and zircon was immersed in 3.5 M HNO_3, ultrasonically cleaned for an hour, and fluxed on a hotplate at 80°C for an hour. The HNO_3 was removed, and zircon was rinsed twice in ultrapure H_2O before being reloaded into the 300 µl Teflon PFA microcapsules (rinsed and fluxed in 6 M HCl during sonication and washing of the zircon) and spiked with the Boise State University mixed ^{233}U-^{235}U-^{205}Pb tracer solution (BSU-1B). Zircon was dissolved in Parr vessels in 120 µl of 29 M HF with a trace of 3.5 M HNO_3 at 220°C for 48 hours, dried to fluorides and re-dissolved in 6 M HCl at 180°C overnight. The U and Pb were separated from the zircon matrix using an HCl-based anion-exchange chromatographic procedure (Krogh, 1973), eluted together and dried with 2 µl of 0.05 N H_3PO_4.

The Pb and U were loaded on a single outgassed Re filament in 5 µl of a silica-gel/phosphoric acid mixture (Gerstenberger and Haase, 1997), and U and Pb isotopic measurements made on a GV Isoprobe-T multicollector thermal ionization mass spectrometer equipped with an ion-counting Daly detector. The Pb isotopes were measured by peak-jumping all isotopes on the Daly detector for 160 cycles, and corrected for 0.16 ± 0.03%/a.m.u. or 0.18 ± 0.03%/a.m.u. (1σ) mass fractionation. Transitory isobaric interferences due to high-molecular weight organics, particularly on ^{204}Pb and ^{207}Pb, disappeared within approximately 60 cycles, while ionization efficiency averaged 10^4 cps/pg of each Pb isotope. Linearity (to ≥1.4 x 10^6 cps) and the associated deadtime correction of the Daly detector were determined by analysis of NBS982. Uranium was analyzed as UO_2^+ ions in static Faraday mode on 10^{12} ohm resistors for 300 cycles, and corrected for isobaric interference of $^{233}U^{18}O^{16}O$ on $^{235}U^{16}O^{16}O$ with an $^{18}O/^{16}O$ of 0.00206. Ionization efficiency averaged 20 mV/ng of each U isotope. Uranium mass fractionation was corrected using the known $^{233}U/^{235}U$ ratio of the Boise State University tracer solution.

The U-Pb dates and uncertainties were calculated using the algorithms of Schmitz and Schoene (2007), calibration of BSU-1B tracer solution of $^{235}U/^{205}Pb$ of 77.93 and $^{233}U/^{235}U$ of 1.007066, $^{238}U/^{235}U$ of 137.818 (Hiess et al., 2012), and U decay constants recommended by Jaffey et al. (1971). The $^{206}Pb/^{238}U$ ratios and dates were corrected for initial ^{230}Th disequilibrium using $D_{Th/U}$ = 0.20 ± 0.05 (1σ) and the algorithms of Crowley et al. (2007), resulting in an increase in the $^{206}Pb/^{238}U$ dates of ~0.09 Ma. All common Pb in analyses was attributed to laboratory blank and subtracted based on the measured laboratory Pb isotopic composition and associated uncertainty. Uranium blanks are estimated at 0.013 pg.

Weighted mean $^{206}Pb/^{238}U$ dates are calculated from equivalent dates (pof >0.05) using Isoplot 3.0 (Ludwig, 2003). Errors on weighted mean dates are given as ± x / y / z, where x is the internal error based on analytical uncertainties only, including: counting statistics, subtraction of tracer solution, and blank and initial common Pb subtraction; y includes the tracer calibration uncertainty propagated in quadrature; and z includes the ^{238}U decay constant uncertainty propagated in quadrature. Internal errors should be considered when comparing the dates with $^{206}Pb/^{238}U$ dates from other laboratories that used the same tracer solution or a tracer solution that was cross calibrated using EARTHTIME gravimetric standards. Errors

including the uncertainty in the tracer calibration should be considered when comparing the dates with those derived from other geochronological methods using the U-Pb decay scheme (e.g., laser ablation ICP-MS). Errors including uncertainties in the tracer calibration and ^{238}U decay constant (Jaffey et al., 1971) should be considered when comparing the dates with those derived from other decay schemes (e.g., $^{40}Ar/^{39}Ar$, ^{187}Re-^{187}Os). Errors are at 2σ.

Biostratigraphy

Limestone, limestone debris flows, dolostone, calcareous siltstone and chert were collected for the determination of fossil ages (Table 2). Fossil reports are included in Appendix B.

Whole-rock lithogeochemistry

Basalt, gabbro and volcaniclastic rock samples along the Dawson fault were analyzed for whole-rock major and trace element geochemistry at both Activation Laboratories (Actlabs) and ALS Laboratories (ALS) (Appendix C, Tables C1-C2). Samples from 2011 to 2018 were prepared and analyzed at Actlabs in Ancaster, Ontario, Canada. Samples were crushed to a -2 mm fraction and then pulverized using a mild steel mill until 95% passed through a 105 µm sieve. The pulps were digested using a lithium metaborate/tetraborate fusion followed by acid dissolution to ensure refractory elements were completely dissolved. Analysis of both major and trace elements were carried out using an ICP-MS. Samples collected in 2019 to 2022 were analyzed for major and trace elements at ALS Laboratories in North Vancouver, British Columbia (BC), Canada. Samples were initially prepared by removing all weathered surfaces and veins using a rock saw. Major elements were analyzed by fused disc XRF, volatile trace elements by aqua regia digestion and ICP-MS, and Ag, Cd, Co, Cu, Li, Mo, Ni, Pb, Sc, Zn by four acid digest and inductively coupled plasma atomic emission spectroscopy (ICP-AES). The USGS certified reference materials (LK-NIP-1) were inserted approximately every 10 samples and blank samples were included in each run.

Precision of the geochemical data was measured using percent relative standard deviation. The values were calculated using:

$$\%RSD = 100\% \times S_i/\mu_i$$

- S_i = mean value of element i over a series of analytical runs
- μ_i = standard deviation of the mean from the series of analytical runs for element i

Accuracy was calculated using percent relative difference using:

$$\%RD = 100\% \times (\mu_i - STD_i)/STD_i$$

- μ_i = mean value of element i in the standard over a number of analytical runs
- STD_i = certified value of element i in the standard or reference material

Precision ranges from 1 to 8% relative standard deviation and accuracy from 0 to 13% relative difference for elements used in the interpretation of the volcanic rocks (Appendix C, Table C3; Jenner, 1996). An interlaboratory comparison between Actlabs and ALS shows that major and trace element variation is ≤5 and ≤12%, respectively, except for elements with concentrations close to the detection limit (e.g., Pb; Cobbett et al., 2023).

Table 2. *Compilation of fossil age constraints for samples collected from sedimentary rocks interbedded with, or enclosing, volcanic rocks and gabbro.*

Sample	Type	Broad age	Confidence	Map label
19RC085-1	orthid brachiopods	Ordovician to Silurian	low	**1**
19RC089-1	solitary rugose coral, disarticulated brachiopod	Silurian or Devonian	low	**2**
19RC106-1	Didymograptus s.l., Phyllograptus sp., Isograptus cf. victoriae lunatus	late Early Ordovician likely	high	**3**
19RC113-1	parvicostellate brachiopod, trilobite pygidium	Ordovician to Silurian		**4**
19RC149-2	coral, orthid and strophomenoid brachiopods, pseudophorid gastropod, crinoid	Ordovician to Devonian		**5**
19RC150-1	ramniform elements	Paleozoic		**6**
19RC158-1	*Stimulograptus* sp., likely *S. sedgwickii* or *S. halli*, *gryptograptus* sp., *Parapetalolithus cf. gigantues*	Darwillian - early Sandbian	high	**7**
20RC003-1	Ptychopleurella sp.	Lower Ordovician to Lower Devonian		**8**
20RC008-1	Catenipora sp., undetermined solitary rugose corals, Palaeophyllum, P. rugosum, and *Maclurites* sp.	Late Ordovician		**9**
20RC018-1	Byssonychia	Late Ordovician		**10**
20RC032-1	Orthograptus calcaratus, Climacograptus bicornis, Cryptograptus marcidus, Archiclimacograptus antiquus, Dicranograptus sp. (possibly D. brevicaulis), Dicranograptus nicholsoni	Late Ordovician		**11**
20RC041-2	*Aphelognathus* sp., *Panderodus unicostatus* (Branson & Mehl) or *Panderodus gracilis* (Branson & Mehl), *Pseudobelodina quadrata* Sweet 1979, *Pseudobelodina* sp., indeterminate ostracodes	Late Ordovician	high	**12**
20RC044	undetermined solitary rugose corals, Amblyosiphonella or Amblyosiphonelloides sp. 1 (sphinctozoan sponge); and an asaphid trilobite.	Late Ordovician	high	**13**
20RC045	Trilobites: illaenid trilobite (possibly Stenopareia), Failleana, asaphid trilobite, harped trilobite; Brachiopods: Strophomena sp., fenesteillid bryozoans.	Late Ordovician	high	**14**
20RC046-1	undetermined strophomenid brachiopod, undetermined stropheodontid brachiopod, unidentified rhynchonellid brachiopod, possibly Hypsiptycha, Amblyosiphonella or Amblyosiphonelloides sp. 2, illaenid trilobite belonging to the genus Stenopareia Holm, 1886, *Maclurites* sp., Loxonema sp., the cyrtoconid nautiloid genus Winnipegoceras.	Late Ordovician	high	**15**
20RC047-1	Either a small Plaesiomys, or a dalmanelloid brachiopod, Strophomena sp. 1, Strophomena sp. 2.	Late Ordovician		**16**
20RC050-2	Orthograptus expansus, Orthograptus calcaratus (subspecies indet.), Pronormalograptus euglyphus, Archiclimacograptus meridionalis, Archiclimacograptus modestus, Jianxigraptus gurleyi, Jiangxigraptus sextans?, Glossograptus sp., Thamnograptus capillaris, Reteograptus sp.	Upper Sandbian	high	**17**
20RC069-1	*Panderodus unicostatus* (Branson & Mehl) or *Panderodus gracilis* (Branson & Mehl)	Ordovician - Devonian		**18**
20RC167-1	Indeterminate fasciculate rugose coral	Middle Ordovician or younger		**19**
21RC101-1	*Pronormalograptus euglyphus*, *Archiclimacograptus cf. meridionalis*, *Jiangixgraptus bispiralis*, *Apoglossograptus uniformis* (= Isograptus lyra of Lenz and Chen, 1985), *Jianxigraptus gurleyi*, *Pseudoazygograptus incurvus*	Late Ordovician		**20**
21RC144-1	small brachiopods *Glyptorthi*, small crinoid columns	probably Late Ordovician	low	**21**
21RC145-1	*Periodon flabellum* (Lindström 1955) (Sb, Sc, Sa, M and P elements), *Protopanderodus parvibasis* Löfgren 1978, *Protopanderodus varicostatus* (Sweet and Bergström 1962), *Pariostodus originalis* (Sergeeva 1963)	Middle Ordovician	high	**22**
21RC146-2	*Periodon flabellum* (Lindström 1955) (Sb, Sc, Sa, M and P elements), *Protopanderodus parvibasis* Löfgren 1978, *Protopanderodus varicostatus* (Sweet and Bergström 1962), *Pariostodus originalis* (Sergeeva 1963)	Middle Ordovician	high	**23**
21RC205-1	*Inanigutta* sp., ? *Involuentactinia* sp., ? *Maletzella* sp., rare sponge spicules, rare pyrite crystals	Ordovician-Silurian	high	**24**
21RC240-1	*Psigraptus* sp., *Rhabdinopora flabelliformus norvegica* ?, *Adelograptus tenellus*, *Anisograptus* sp.	Early Ordvician	high	**25**
21RC237-1	*Inanigutta* sp., *Secuicollacta* sp., *Zaddrappolus* sp., sponge spicules (hexacttinellids), rare pyrite crystals	middle-late Silurian	high	**26**
21RC255-1	*Secuicollacta* sp., sponge spicules, rare pyritized radiolarians	late Ordovician-late Silurian		**27**
22RC003-2-1	*Maclurites* sp., solitary rugose corals, *Paleofavosites* sp. (favositid coral), orthoconic cephalopods	Late Ordovician	med	**28**
22RC024-1	*Maclurites* sp., *Trochonema* sp., indeterminate orthid brachiopod, undetermined orthoconic cephalopods, large solitary, rugose coral, crinoid ossicles, indeterminate tubes	Late Ordovician		**29**
22RC037-1	Acodus? sp., Drepanodus sp., Sponge spicules	possibly late Tremadocian	low	**30**
22RC044-1	Acanthodus? sp., Drepanodus sp., Oistodus? sp. s.f., Teridontus? sp., Variabiloconus? sp., paraconodonts, Fragmentary inarticulate brachiopods	Early Ordovician	med	**31**
J1520	*Kormagnostus seclusus* Resser, *Genevievella simon*, *Matania aff. M. matuta*	base of the Guzhangian Stage		**32**
J1521		Miaolingian		**33**
J1523	*Kormagnostus seclusus* Resser, *Hysteropleura schucherti*, *Coenaspis spectabilis* Resser, *Cedaria cf. C. tumicephala*	base of the Guzhangian Stage		**34**
82-TW-160		Caradocian or Ashgillian		n/a

Whole-rock Hf and Nd isotope geochemistry

Whole-rock Hf and Nd isotope ratios were measured at Pacific Centre for Isotope and Geochemical Research (PCIGR) using separate aliquots of sample powders used for trace element analyses (Appendix C, Table C4). Nd and Hf were purified using sequential ion-exchange column chemistry. Separation procedures for Nd followed Weis et al. (2006, 2007). Hafnium separations were conducted using TODGA resin following a method modified after Connelly et al. (2006). The Nd and Hf isotope ratios were measured by multicollector inductively coupled plasma mass spectrometry (Nu Instruments Ltd., Nu II 214 or Nu 1700) following Weis et al. (2006, 2007), and normalized to the JNDi (Nd) and JMC 475 (Hf) standards using sample-standard bracketing. Normalization values are $^{143}Nd/^{144}Nd = 0.512116$ for JNDi (Tanaka et al., 2000) and $^{176}Hf/^{177}Hf = 0.282160$ for JMC 475 (Blichert-Toft et al., 1997). Repeat analyses of the JNDi and JMC 475 standards during two sample batches in 2020 yielded mean isotopic compositions of $^{143}Nd/^{144}Nd = 0.512101 \pm 0.000008$ (2SE, n = 11), and $^{176}Hf/^{177}Hf = 0.282167 \pm 0.000006$ (2SE, n = 22) and 0.282177 ± 0.000004 (2SE, n = 5), respectively.

Reference materials analyzed in this study include BCR-2 for Nd, and BCR-2 and G-3 for Hf. Analysis of BCR-2 resulted in isotopic compositions of $^{143}Nd/^{144}Nd = 0.512641 \pm 0.000008$ to 0.512643 ± 0.000007 (2SE, 6 to 9 ppm) and $^{176}Hf/^{177}Hf = 0.282874 \pm 0.000006$ to 0.282872 ± 0.000004 (2SE, 7 to 14 ppm), in good agreement with lab average values (Appendix C, Table C4). Measurement of G-3 yielded values of $^{176}Hf/^{177}Hf = 0.282512 \pm 0.000001$ (2SE, 22 ppm) that overlap with the lab average and values by Weis et al. (2006, 2007). Reproducibility was also monitored by the use of numerous replicate aliquots and duplicate samples, which were overall excellent with values less than 9 ppm for Nd and 31 ppm for Hf (Table C4). All reference data presented as comparison fields have been re-normalized to the accepted values of JNDi and JMC 475 as above. The present-day CHUR values used include $^{143}Nd/^{144}Nd = 0.512638$ (Blichert-Toft and Albarède, 1997) and $^{176}Hf/^{177}Hf = 0.282785$ (Bouvier et al., 2008), and parent-daughter ratios are $^{147}Sm/^{144}Nd = 0.1967$ (Jacobsen and Wasserburg, 1980) and $^{176}Lu/^{176}Hf = 0.0336$ (Bouvier et al., 2008).

Results

Volcanic rocks and gabbro intrusions along the Dawson fault form two distinct groups: 1) Cambrian rocks that occur mostly south of the Dawson fault; and 2) Upper Ordovician rocks north of the Dawson fault. Field observations and analytical results are presented from west to east for each age group below.

Cambrian igneous rocks along the Dawson fault

Cambrian volcanic rocks that occur along the Dawson fault corridor were collected for geochemical and geochronological analyses from the Dempster and McKay Hill areas, the basal Bouvette Formation near Castle Mountain and Nadaleen River area and from within the Dawson fault zone near the Nadaleen River (Fig. 2).

Dempster area

In 2015, the Yukon Geological Survey (YGS), in collaboration with Dartmouth College, investigated mafic igneous rocks exposed south of the Dawson fault west and east of the Dempster Highway (NTS 116BC; Figs. 2 and 4). The Dempster volcanic rocks crop out along the western end of the fault for approximately 200 km from the Alaska-Yukon border to

Rae Creek (Fig. 4; Thompson et al., 1994; Strauss et al., 2014). These volcanic rocks occur unconformably above the Hyland Group and cogenetic gabbro intrudes the Hyland Group (Strauss et al., 2014). Gabbro and basalt were sampled throughout the region, and the Fifteen Mile area was mapped in detail and sampled systematically for this study (Fig. 5). Mafic volcanic rocks are mapped in three parts of the stratigraphy in the Fifteen Mile area (CG, COv, Ov; Fig. 5). Collectively this group of rocks yields basaltic Zr/Ti ratios from 0.0094 to 0.0304 (Fig. 6a-b; Appendix C, Table C1). The rocks are alkaline to ultra-alkaline based on elevated Nb/Y ratios from 0.754 to 3.60 (Fig. 6a-b). Chromium and Ni concentrations range from 10 to 650 ppm and from 5 to 750 ppm, respectively, except for two samples that have Cr values over 1000 ppm (Appendix C, Table C1). These rocks have elevated TiO_2 (0.65–3.68%) relative to primitive mantle TiO_2 values (0.22%) and a large range in Al_2O_3/TiO_2 ratios (3–12 wt%). The P_2O_5 values range from 0.2 to 1.7 wt%. Compared to the primitive mantle, the Dempster volcanic rocks have strong light rare earth element (LREE) enrichment (La_{pm}/Sm_{pm} = 2.28 to 4.23) and heavy rare earth element (HREE) depletion relative to middle rare earth elements (MREE) (Sm_{pm}/Yb_{pm} = 2.28 to 10.40; Fig. 6a-b). The Dempster volcanic rocks yield εNd_{500} = -0.2 to -2.5 (Fig. 7).

Limestone debris flows interbedded with mafic volcanic rocks in the west Dempster area contain upper Cambrian (Miaolingian) trilobite fragments that constrain the age of the Dempster volcanic rocks in this area (Fig. 8; J1520 and J1523; Table 2). *Kormagnostus seclusus* Resser, agnostoid species present in two separate collections, range through the *Cedaria minor* and *Cedaria selwyni* zones (Pratt, 1991). A basal *Cedaria* Zone assignment for J1523 is consistent with the occurrence of both *Hysteropleura schucherti* and *Coenaspis spectabilis* Resser in the sample (Rasetti, 1966). This places the trilobite-bearing strata in the global

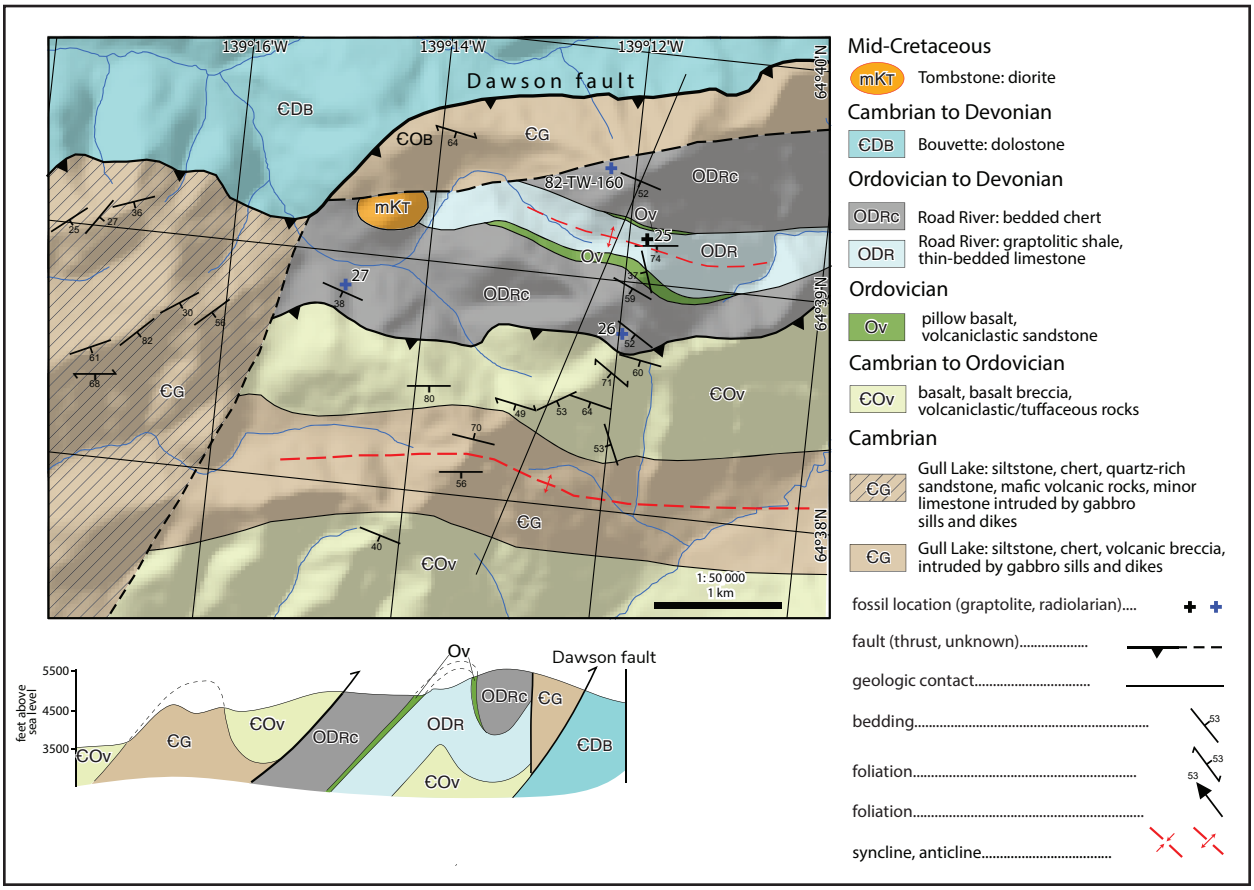

Figure 5. *Bedrock geology map and cross section of the Fifteen Mile River, south of Dawson fault segment 1 (Yukon Geological Survey, 2024).*

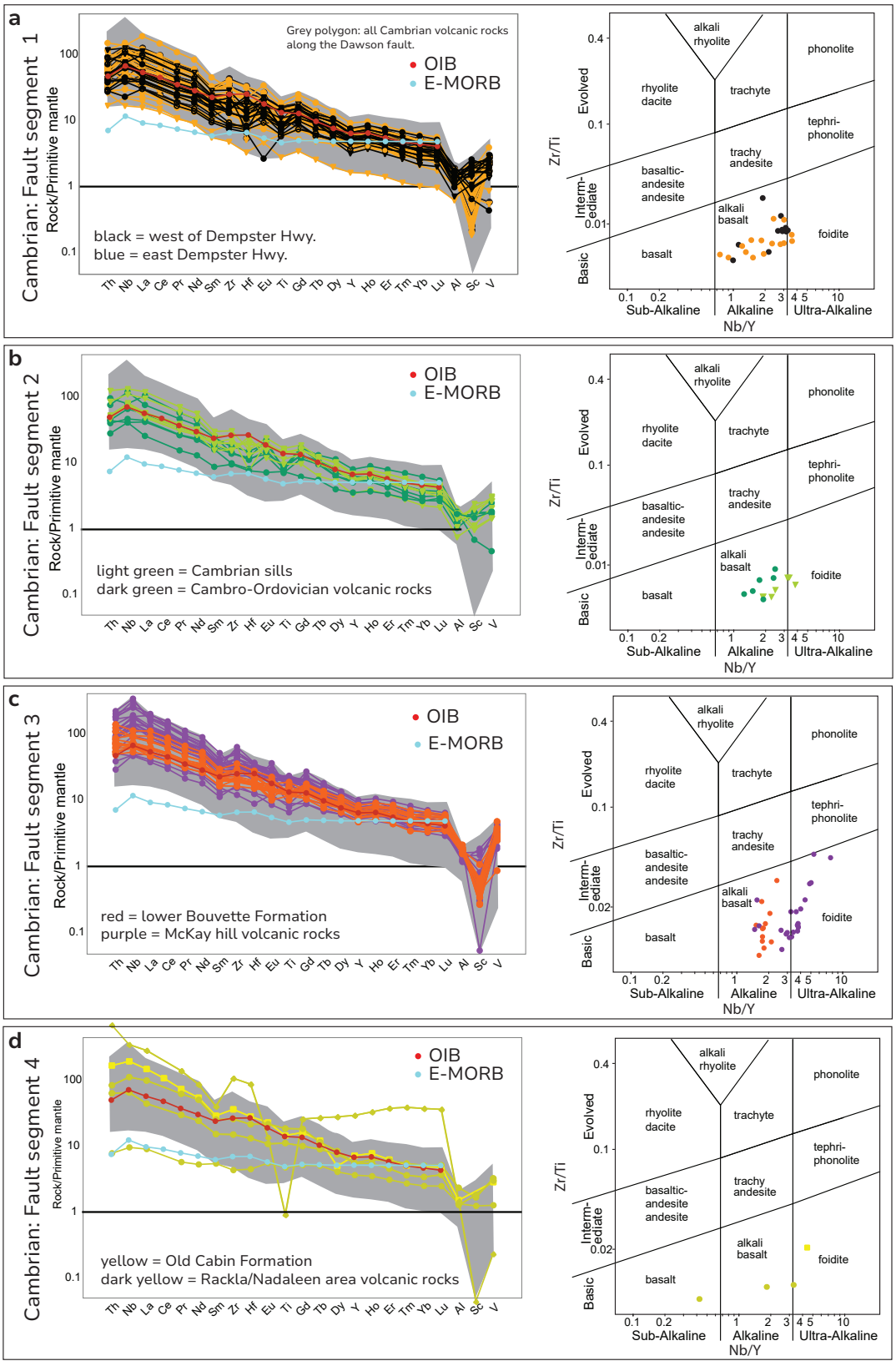

Figure 6. *Lower Cambrian volcanic rocks plotted on Zr/Ti versus Nb/Y discrimination diagram of Pearce (1996) suggesting they are predominantly alkaline to ultra-alkaline basic rocks. Lower Cambrian volcanic rocks plotted on primitive mantle normalized plots using immobile elements of Sun and McDonough (1989). Grey polygon shows the chemistry of all of the lower Cambrian rocks along the Dawson fault; (a-d) Data sub-divided by location along the Dawson fault:* **(a)** *West Dempster area;* **(b)** *East Dempster area;* **(c)** *McKay Hill and Lower Bouvette near Carpenter Ridge;* **(d)** *Rackla and Nadaleen areas and east of the end of the Dawson fault.*

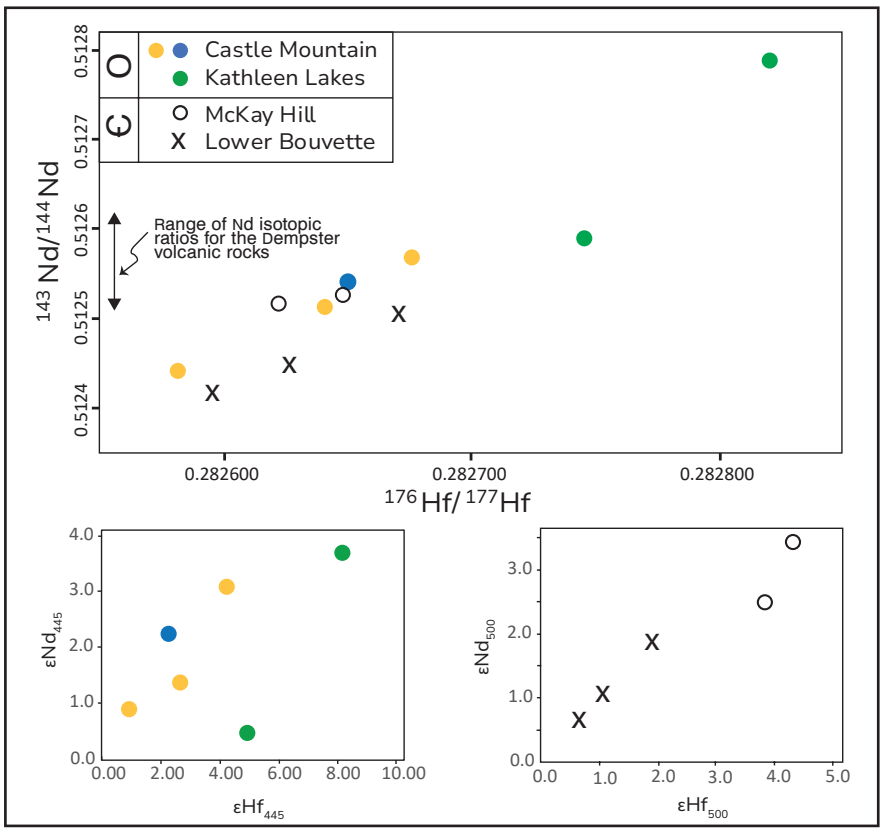

Figure 7. *$^{143}Nd/^{144}Nd$ versus $^{176}Hf/^{177}Hf$ of both Upper Ordovician and mid-lower Cambrian volcanic rocks along the Dawson fault. Initial εHf and εNd for Upper Ordovician (ca. 445 Ma) volcanic rocks near Castle Mountain and Kathleen Lakes areas. Initial εHf and εNd for lower Cambrian (ca. 500 Ma) volcanic rocks from the McKay Hill and Carpenter Ridge areas.*

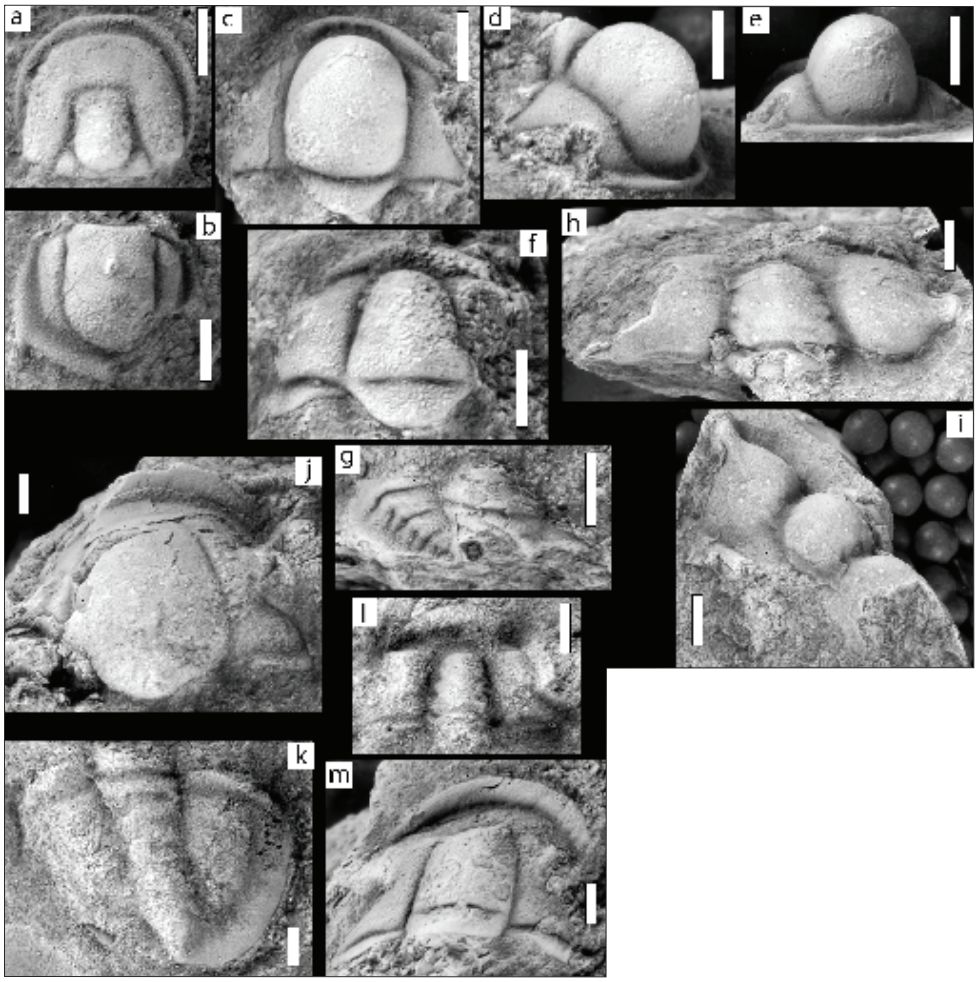

Figure 8. *Middle Cambrian (lower Cedaria Zone) agnostoid and trilobite species recovered from carbonate interbedded with volcanic rocks along Dawson fault segment 1 .* ***(a,b)*** *Kormagnostus seclusus YG 921.1, YG 921.2;* ***(c,d,e)*** *Matania aff. M. matuta YG 921.5;* ***(f,g)*** *Genevievella simon YG 921.3, YG 921.4;* ***(h,i)*** *Coenaspis spectabilis YG 922.5;* ***(j)*** *Cedaria cf. C. tumicephala YG 922.4;* ***k,m)*** *Cedaria spp. YG 922.2, YG 922.3;* ***(l)*** *Hysteropleura schucherti YG 922.1. All dorsal views, except d) and i) (anterior oblique) and e) (anterior). All cranidia except b), d), and i), which are pygidia. Scale bars represent 1 mm.*

chronostratigraphy at the very near the base of the Guzhangian Stage, the uppermost of three global stages recognized within the Miaolingian Series.

McKay Hill area

Detailed mapping (1:25 000 scale) of mafic volcanic rocks exposed in the McKay Hill area was carried out as part of a larger targeted study to characterize lower Paleozoic volcanic rocks exposed in the Yukon and western NWT (Figs. 2 and 9). Basalt, basalt breccia and volcaniclastic rocks are interbedded with chert, sandstone and shale at McKay and Sullivan hills, south of the Dawson fault in north-central Yukon (Fig. 9; Cobbett, 2022). Collectively the volcanic rocks have basaltic Zr/Ti ratios of 0.0092 to 0.031 (Fig. 6c). The rocks are alkaline to ultra-alkaline based on elevated Nb/Y ratios of 1.48 to 7.68. Chromium and Ni concentrations range from 5 to 630 ppm and from 3 to 347 ppm, respectively, except for two samples that have Cr values over 700 ppm (Appendix A, Table A2). These rocks have elevated TiO_2 (1.88–5.03%) relative to primitive mantle TiO_2 values (0.22%) and a large range in Al_2O_3/TiO_2 ratios (2.31–8.45 wt%; except three samples that have values >15 wt%). The P_2O_5 values range from 0.34 to 1.44 wt%. Compared to the primitive mantle, the McKay Hill volcanic rocks have strong LREE enrichment (La_{pm}/Sm_{pm} = 3.03 to 5.94) and HREE depletion relative to MREE (Sm_{pm}/Yb_{pm} = 2.54 to 9.97; Fig. 6c). The McKay Hill volcanic rocks samples yield $\varepsilon Nd_{49}8$ = +2.7 to +3.2 and εHf_{498} = +4.0 to +4.2 (Fig. 7).

Coarse-grained volcaniclastic rock comprising 4 to 32 mm wide clasts of chlorite-altered mafic volcanic rock and scoria, and fragments of pyroxene crystals in a calcite matrix, were collected north of McKay Hill for zircon U-Pb geochronology (20RC142-1; Figs. 9 and 10a). Angular and commonly jagged-edged, oscillatory-zoned, equant zircon grains range in size from 50 to 150 µm (Appendix A, Fig. A1). Forty-two zircon grains yielded individual $^{206}Pb/^{238}U$ LA-ICP-MS dates of 583 ± 51 to 470 ± 16 Ma (Fig. 11; Appendix A, Table A1). Five grains analyzed by CA-ID-TIMS yielded a weighted mean $^{206}Pb/^{238}U$ date of 498.54 ± 0.15(0.21)[0.56] Ma interpreted to be the crystallization age of the volcanic rocks (mean square of weighted deviation [MSWD] = 1.3, pof = 0.30; Table 1; Fig. 12a).

Coarse-grained sandstone with sub-angular to angular grains of calcite, chlorite-altered basalt and minor quartz in a fine-grained matrix yielded rounded to euhedral zircon grains with dominantly oscillatory zoning (20RC092-1; Fig. 10b). The zircon grains range in size from 40 to 80 µm with aspect ratios of 1:2 to 1:4. Fifty-nine zircon grains from this sample yielded individual $^{206}Pb/^{238}U$ LA-ICP-MS dates of 3057 ± 62 to 1022 ± 24 Ma and one zircon grain that yielded a date of 509 ± 28 Ma (Fig. 11; Appendix A, Table A1). The youngest zircon was analyzed by CA-ID-TIMS and yielded an individual $^{206}Pb/^{238}U$ date of 497.57 ± 0.70 Ma interpreted as the maximum depositional age of the sandstone (Table 1).

Carpenter Ridge

Volcaniclastic sandstone, conglomerate and basalt of the lower Bouvette Formation crop out along two ridges south of Carpenter Creek to the north of McKay Hill and on the north side of the Dawson fault (Fig. 9). Thick beds of polymictic conglomerate dominate the basal 50 m of the volcanic succession with minor basalt succeeded by 60 m of basalt and basalt breccia (Fig. 13a). The uppermost 30 m comprises carbonate and fine-grained clastic rocks interbedded with basalt and capped by volcanogenic conglomerate. Basalt from this succession has basaltic Zr/Ti ratios of 0.001 to 0.4 (Fig. 6c). The rocks are alkaline to ultra-alkaline based on elevated Nb/Y ratios (1.6–2.1). Chromium and Ni concentrations range from 5 to 420 ppm and from 3 to 140 ppm, respectively, except for one sample that has Cr values

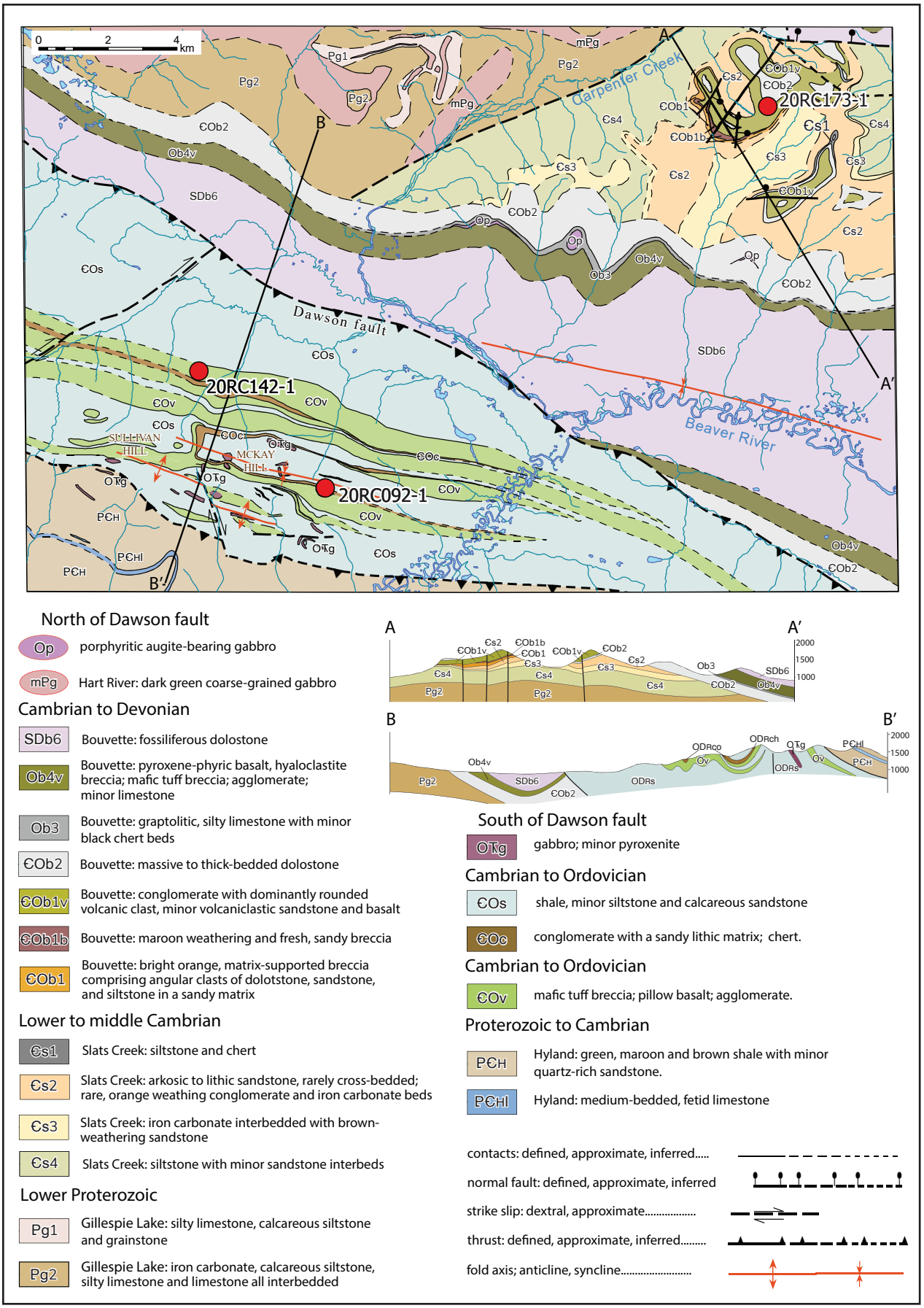

Figure 9. *Bedrock geology map and cross sections of the McKay Hill and Carpenter Ridge areas along the Dawson fault segment 3.*

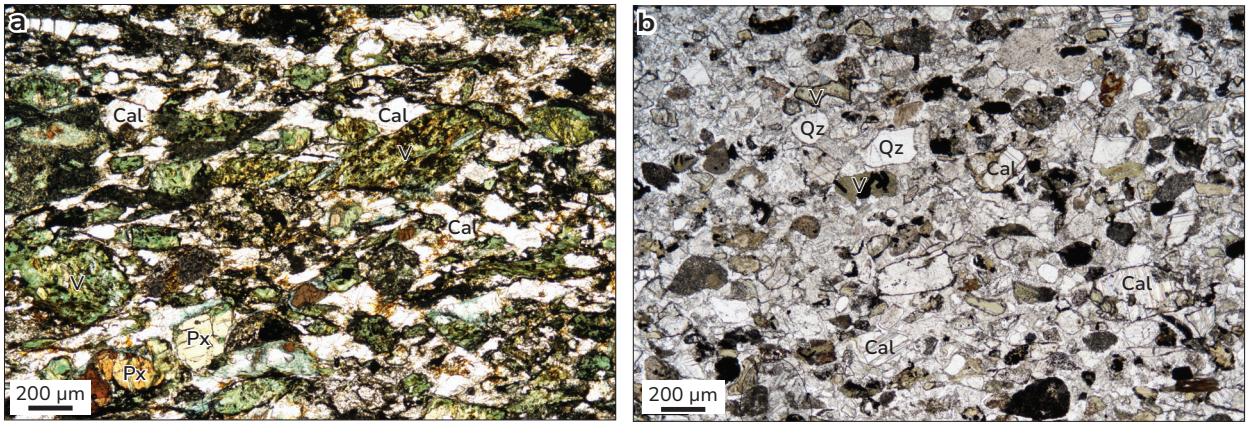

Figure 10. *Thin section micro-photographs of samples collected at McKay Hill for U-Pb dating.* ***(a)*** *Crystal-rich, volcaniclastic sandstone comprising altered grains of basalt (green clasts) and pyroxene crystals (brown and beige clasts) in a calcite matrix. Cal – calcite, V – volcanic rock.* ***(b)*** *Sandstone comprising angular to sub-rounded grains of calcite (Cal), altered volcanic rocks (V), and quartz (Qz) in a calcite matrix.*

over 700 ppm and two samples that have Ni values over 200 (Appendix A, Table A2). These rocks have elevated TiO_2 (0.3–4.4%) relative to primitive mantle TiO_2 values (0.22%) and a large range in Al_2O_3/TiO_2 ratios (3-16 wt%; except two samples that have values >25 wt %). The P_2O_5 values range from 0.06 to 1.2 wt%. Compared to the primitive mantle, the lower Bouvette volcanic rocks have strong LREE enrichment (La_{pm}/Sm_{pm} = 2.3 to 4.7) and HREE depletion relative to MREE (Sm_{pm}/Yb_{pm} = 2.9 to 6.7; Fig. 6c). The lower Bouvette Formation samples yield εNd_{500} = +0.7 to +1.9 and εHf_{500} = +2.6 to +4.0 (Fig. 7).

Quartz-rich wacke at the top of the mafic volcanic and volcaniclastic succession contains sub-angular to sub-rounded quartz, chert, feldspar, shale and basalt grains that range from 0.05 to 7 mm (20RC173-2; Fig. 13b). The rock is slightly effervescent from sparry calcite cement. Well-rounded, equant zircon grains and elongated subhedral zircon grains with aspect ratios of 1:3 to 1:4, range from 60 to 180 µm (Appendix A, Fig. A1). Both groups contain zircon with oscillatory and sector zoning. Zircon grains (n = 162) yielded individual $^{206}Pb/^{238}U$ LA-ICP-MS dates of 3341 ± 103 to 468 ± 17 Ma (Fig. 11; Appendix A, Table A1). Seven of the youngest zircon grains were analyzed by CA-ID-TIMS and yielded individual dates of 507.05 ± 0.34, 506.92 ± 0.34, 505.75 ± 0.34, 500.69 ± 0.33, 499.08 ± 0.26, 495.05 ± 0.33 and 486.48 ± 0.25 Ma (Table 1). The youngest grain provides a maximum depositional age for the sandstone.

Rackla and Nadaleen areas

A mapping project carried out by the YGS between 2019 and 2023 focused on an area north of the Dawson fault centred on Rusty Mountain (NTS 106C04; Fig. 14; Ambrose, 2021, 2022; Ambrose and Bowie, 2020). Samples of lower Paleozoic volcanic rocks that occur as part of the Bouvette Formation exposed north of the Dawson fault were collected for U-Pb geochronology. A conglomerate unit with lenses of volcaniclastic rocks that contain igneous, limestone and chert clasts occurs near Nadaleen Mountain (Fig. 14; Busch et al., 2019). Basalt, ultramafic rocks, and gabbro sills and dikes are mapped between splays of the Dawson fault between the Rackla and Nadaleen rivers (Fig. 15; Colpron, 2012; Colpron et al., 2013).

The geochemical signatures of the volcanic rocks from the Rackla area are based on: 1) two samples of amygdaloidal basalt collected from within strands of the Dawson fault (Fig. 15); 2) one sample of a basalt cobble from Nadaleen Mountain; and 3) one sample of a plutonic

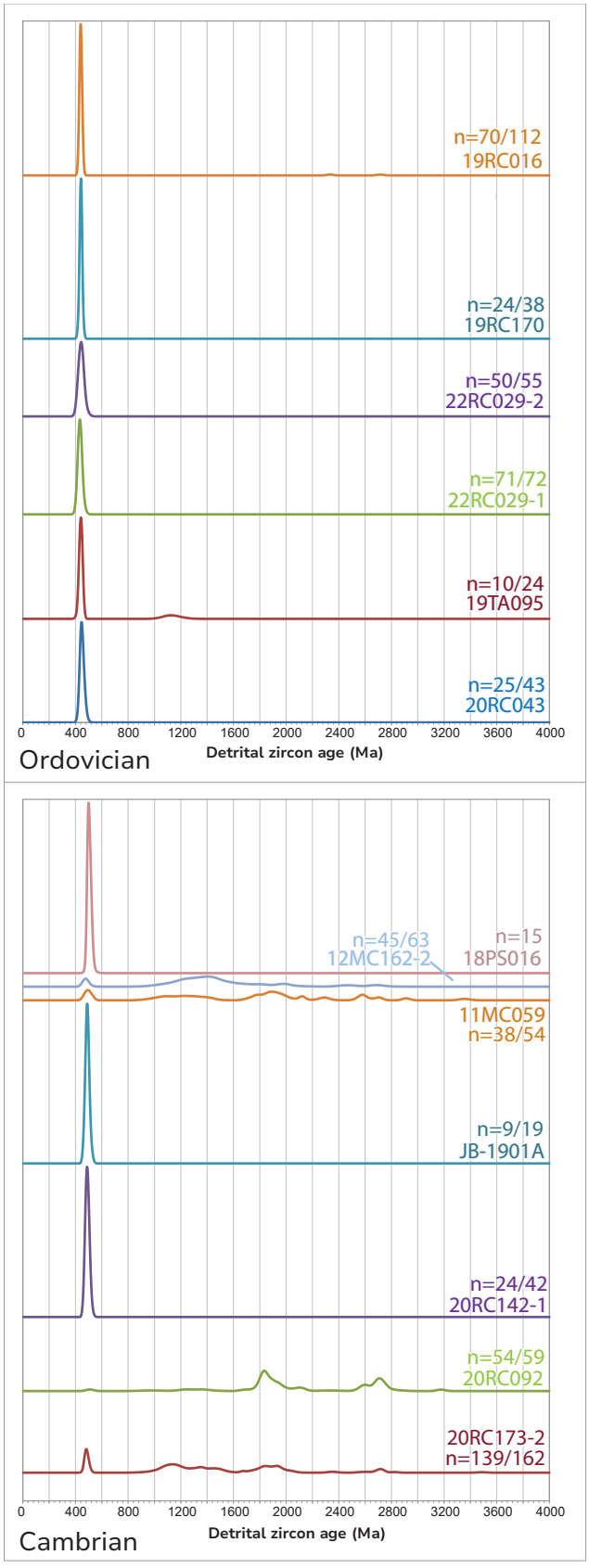

Figure 11. *Probability plots for upper Cambrian and Upper Ordovician volcaniclastic rocks and gabbro. Laser spots that are 1000-0 Ma use $^{206}Pb/^{238}U$ and 1001-2500 Ma spots use $^{207}Pb/^{206}Pb$ ages. Data that has >10% discordance, >5% reverse discordance, or 2σ uncertainty for either the $^{206}Pb/^{238}U$ or $^{207}Pb/^{206}Pb$ isotopic date was >10% were filtered out and not included on the plots.*

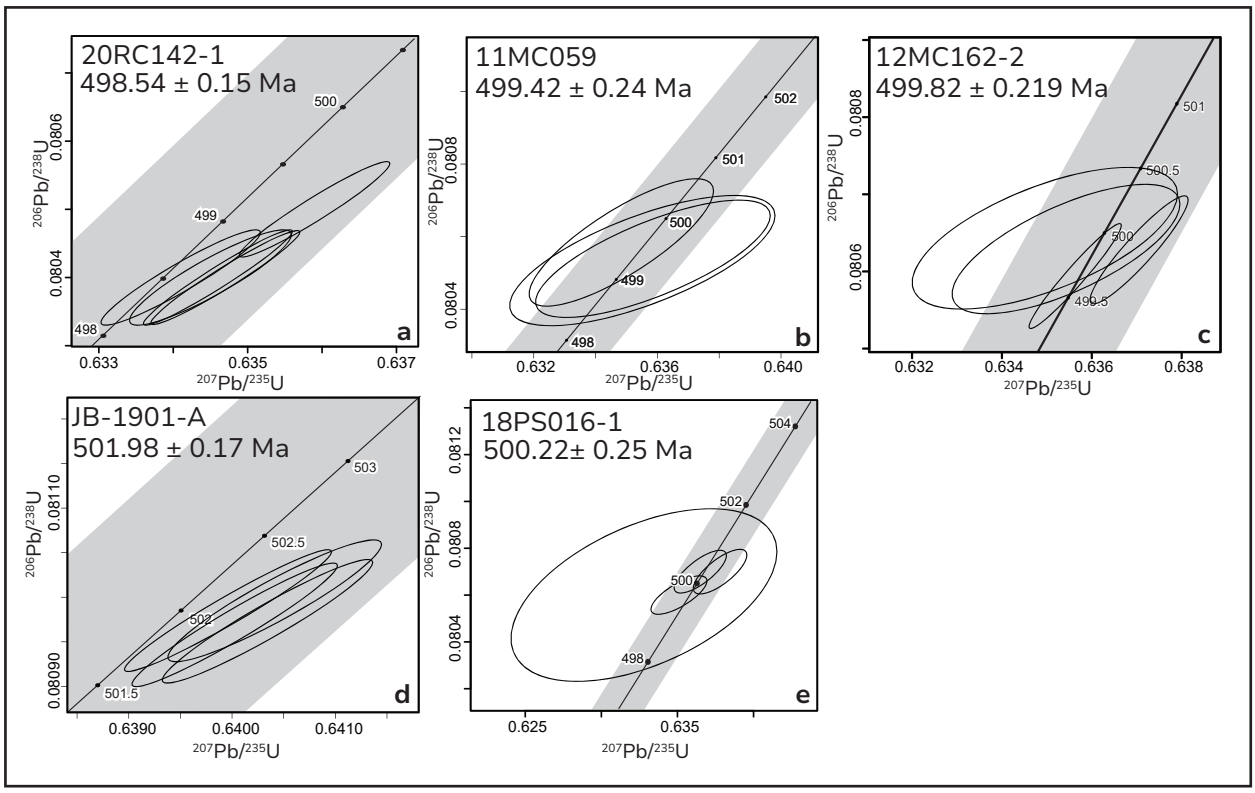

Figure 12. *Concordia plots for upper Cambrian samples dated using CA-ID-TIMS methods.*

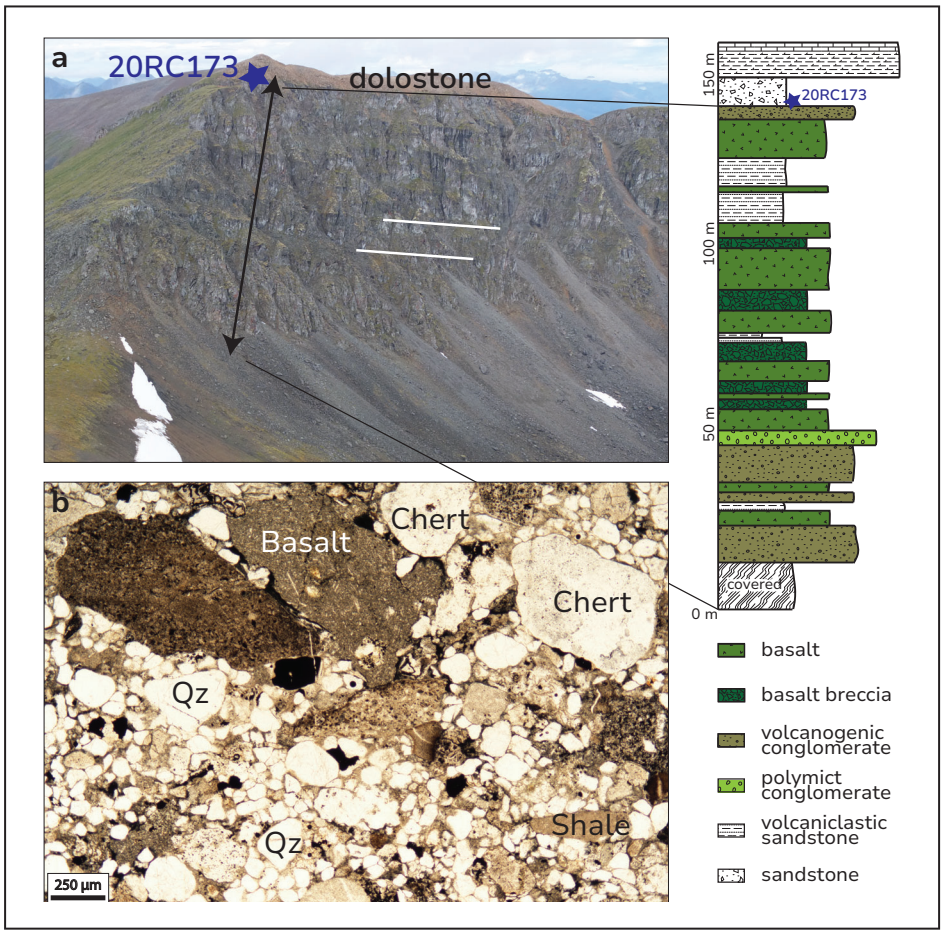

Figure 13. (a) *Mafic volcanic and volcaniclastic succession capped by dolostone. The blue star shows the location of a quartz-rich sandstone that was sampled for U-Pb geochronology. Stratigraphic section through the lower Bouvette volcanic rocks is shown to the right of the photograph.* ***(b)*** *Coarse-grained lithic sandstone from the very top of the stratigraphic section shown in (a) at location of 20RC173. Qz – quartz.*

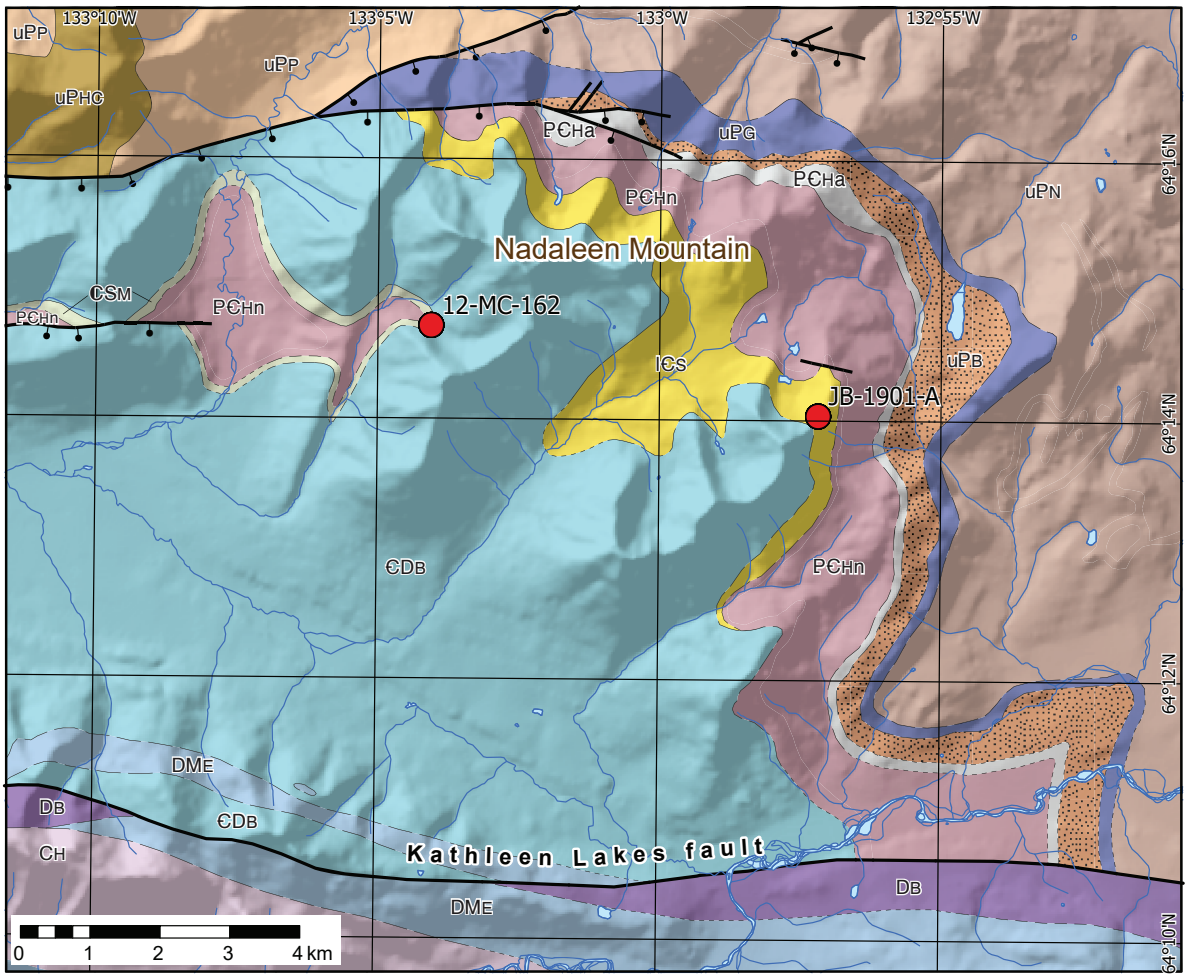

Figure 14. *Bedrock geology map north of the Dawson fault centered on Nadaleen Mountain from segment 4 (Yukon Geological Survey, 2024).*

boulder from a conglomerate from Nadaleen Mountain. The amygdaloidal basalt samples from the fault zone plot in the basalt and alkali basalt fields on a Zr/Ti versus Nb/Y plot (Fig. 6d). The sample of basalt has an E-MORB-like trace element pattern in Figure 6d and notably has

a loss on ignition (LOI) percentage of 18% (Appendix A, Table A2). The alkali basalt sample has primitive mantle normalized trace element patterns similar to ocean island basalt and a LOI of 4% (Fig. 6d). The sample of the basalt cobble from Nadaleen Mountain is alkaline and has primitive mantle normalized trace element patterns similar to ocean island basalt and a LOI of 6%. The plutonic boulder has 70% SiO_2, 0.2% TiO_2 and 0.05% P_2O_5. The sample is enriched in LREE, moderately enriched in HREE compared to primitive mantle, and has a notable positive Zr-Hf anomaly compared to Sm and a negative Ti anomaly (Fig. 6d).

Zircon was separated from a volcaniclastic sandstone collected near the Rackla River within the Dawson fault zone (11MC059; Fig. 15). The zircon has rounded grains with no zoning and elongate to stubby, euhedral grains with oscillatory and sector zoning (Appendix A, Fig. A1). Fifty-four zircon grains yielded individual $^{206}Pb/^{238}U$ LA-ICP-MS dates of 3339 ± 140 to 263 ± 10 Ma (Fig. 11; Appendix A, Table A1). Five of the youngest zircon grains were analyzed by CA-ID-TIMS, three of which yielded a weighted mean date of 499.42 ± 0.24(0.28)[0.59] Ma interpreted as the maximum depositional age of the sandstone (Fig. 12b; Table 1).

The sandy matrix of a conglomerate from the base of the Bouvette Formation near Nadaleen Mountain (12MC162-2) contains euhedral zircon with aspect ratios of 1:1 to 1:3 and oscillatory zoning (Fig. 14). Sixty-three zircon grains yielded individual $^{206}Pb/^{238}U$ LA-ICP-MS dates of 2635 ± 99 to 471 ± 23 Ma (Fig. 11; Appendix A, Table A1). Seven of the youngest zircon grains were analyzed by CA-ID-TIMS, four of which yielded a weighted mean date of 499.82 ± 0.19(0.24)[0.59] Ma (MSWD = 0.5, pof = 0.71; Fig. 12c; Table 1). Several kilometres to the east another sample of a volcanogenic conglomerate with a matrix of basaltic sand and silt contains

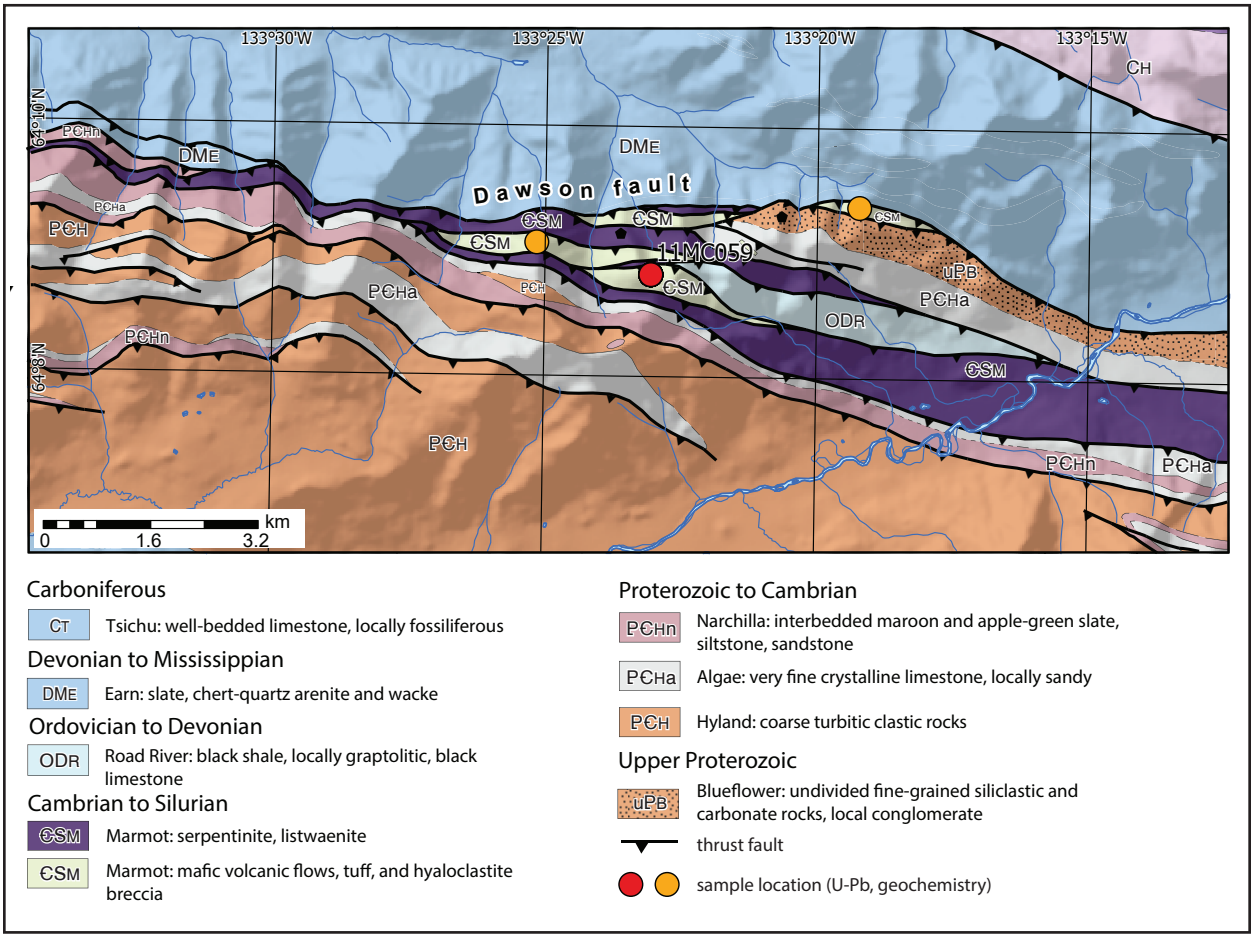

Figure 15. *Bedrock geology map if the Dawson fault zone from fault segment 4 (Yukon Geological Survey, 2024).*

zircon (n = 19) with unimodal age spectrum that yielded individual $^{206}Pb/^{238}U$ LA-ICP-MS dates of 513 ± 16 to 483 ± 18 Ma (JB-1901A; Fig. 11; Appendix A, Table A1). Five of the youngest grains were analyzed by CA-ID-TIMS, four of which yielded a weighted mean date of 501.98 ± 0.17(0.29)[0.60] Ma (MSWD = 0.2, pof = 0.09; Fig. 12d; Table 1).

East end of the Dawson fault

At the easternmost end of the Dawson fault (NTS 106B04), upper Cambrian mafic volcanic and volcaniclastic rocks assigned to the Old Cabin Formation were mapped as part of the Selwyn basin and sampled for zircon U-Pb geochronology (Fig. 16; MacNaughton et al., 2016). Volcaniclastic sandstone mapped as part of the Old Cabin Formation southeast of the eastern end of the Dawson fault has a unimodal zircon peak of 499.89 ± 0.14 Ma (MacNaughton et al., 2016). The Old Cabin Formation volcanic rocks are ultra-alkaline and have trace element patterns similar to ocean island basalt, based on one sample of altered mafic tuff basalt (Fig. 6d). The LOI for the sample is ~24% and it has a Na_2O value of 0.05% (Appendix A, Table A2).

Mafic tuff breccia with angular clasts of altered basalt in a calcite-altered, very fine-grained matrix was collected from an area southeast of the Dawson fault (18PS016-1; Fig. 16). Fifteen zircon grains yielded individual $^{206}Pb/^{238}U$ LA-ICP-MS dates of 518 ± 12 to 495 ± 12 Ma (Fig. 11). Four zircon grains extracted from the sample were analyzed by CA-ID-TIMS and yielded a weighted mean $^{206}Pb/^{238}U$ date of 500.22 ± 0.25(0.34)[0.62] Ma interpreted to the crystallization age of the basalt (MSWD = 1.4, pof = 0.24; Fig. 12e; Table 1).

Upper Ordovician igneous rocks along the Dawson fault

Detailed mapping (1:25 000 and 1:50 000 scale) of mafic volcanic rocks exposed in the Fifteen Mile, Castle Mountain and Kathleen Lakes areas were carried out as part of a larger targeted study to characterize lower Paleozoic volcanic rocks exposed in the Yukon and western NWT.

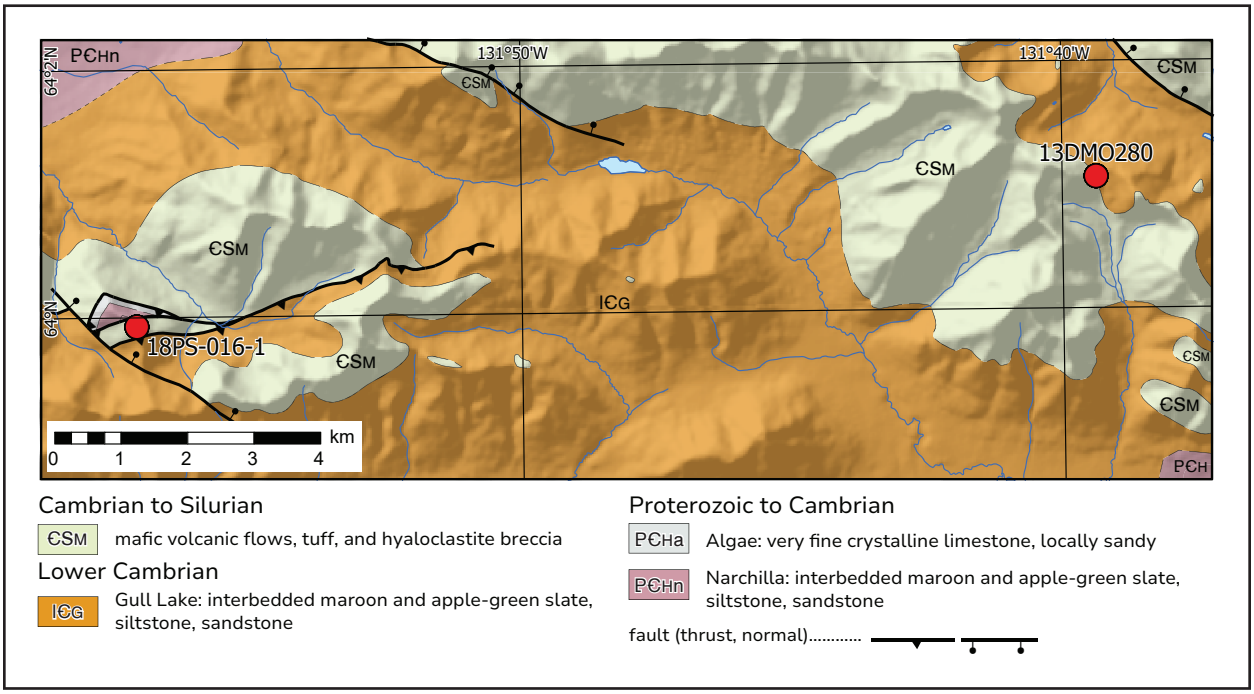

Figure 16. *Bedrock geology map east of the end of the Dawson fault (Yukon Geological Survey, 2024).*

Upper Ordovician volcanic rocks that occur along the Dawson fault corridor are represented by samples collected for geochemical and geochronological analyses from the Castle Mountain area, the Kathleen Lakes area and one location east of Kathleen Lakes (Ambrose and Bowie, 2020). Ordovician to Silurian volcanic rocks were mapped locally near the Fifteen Mile River (Fig. 5) within the west Dempster area (Fig. 4).

Dempster area

A thin band (~50 m) of volcanic and volcaniclastic rock that crops out south of the Dawson fault near the Fifteen Mile River occurs stratigraphically above shale that contains Lower Ordovician graptolites and below chert that contains middle to upper Silurian radiolarians (Fig. 5). The age of some of the volcanic rocks is Ordovician to Silurian based on these fossil age constraints (Table 2; Appendix B).

Castle Mountain area

An interval of mafic volcanic and volcaniclastic rocks occur within the Bouvette Formation near Castle Mountain (Figs. 17 and 18; Cobbett, 2020, 2022). In this area, flows of porphyritic basalt (Fig. 19a) grade laterally to sandstone with basaltic clasts (Fig. 19b). Locally, volcanic breccia form mounds that are flanked by bedded volcaniclastic rocks (Fig. 19c). Collectively these volcanic rocks have basaltic Zr/Ti ratios of 0.009 to 0.03 except for one sample with a ratio of 0.06 (Fig. 20a). The rocks are alkaline to ultra-alkaline based on elevated Nb/Y ratios (1.5–3.5; Fig. 20a). Chromium and Ni concentrations range from 5 to 640 ppm and from 3 to 432 ppm, respectively, except one sample that has Cr values over 800 ppm (Appendix A, Table A3). These rocks have elevated TiO_2 values (1.4–3.7%) relative to primitive mantle TiO_2 values (0.22%) and a large range in Al_2O3/TiO_2 ratios (4–11%). The P_2O_5 values range from 0.1 to 1.5 wt%. Compared to the primitive mantle, the Castle Mountain volcanic rocks have strong LREE enrichment (La_{pm}/Sm_{pm} = 2.6 to 4.4) and HREE depletion compared to MREE (Sm_{pm}/Yb_{pm} = 3.3 to 6.6) except one sample that has a ratio of 9.1 (Fig. 20a). Samples from the Castle Mountain and Kathleen Lakes areas yielded εNd_{450} = +1.0 to +3.1 and εHf_{450} = +0.9 to +4.2, and εNd_{450} = +0.5 to +3.7 and εHf_{450} = +4.9 to +8.2, respectively (Fig. 7).

Four samples of clastic rocks from this sequence were analyzed for U-Pb zircon geochronology. Medium-grained, volcaniclastic sandstone, with maroon and green, rounded basalt clasts, was collected east of Ervin Creek near the top of the basalt unit (20RC043-1 from Ob4v on Figs. 17, 18 and 19d). Elongate zircon crystals with aspect ratios of 1:3 to 1:5 range in size from 40 to 160 µm and most have oscillatory zoning (Appendix A, Fig. A1). Forty-three LA-ICP-MS analyses of 114 zircon grains yielded individual $^{206}Pb/^{238}U$ LA-ICP-MS dates from 477 ± 17 to 430 ± 17 Ma (Fig. 11; Appendix A, Table A1). Five grains analyzed by CA-ID-TIMS yield a weighted mean $^{206}Pb/^{238}U$ date of 453.42 ± 0.14(0.19)[0.53] Ma interpreted to be the crystallization age of the basalt (MSWD = 0.8, pof = 0.52; Fig. 21a; Table 1).

Fine-grained, biotite-bearing sandstone at the very top of the volcanic succession within the middle part of the Bouvette Formation section on the east end of Castle Mountain (19RC170-1 from Ob5 on Figs. 17, 18 and 19e), yielded euhedral, oscillatory zoned, elongate zircons grains with aspect ratios of ~2:1 to 5:1 that range in size from 100 to 300 µm (Appendix A, Fig. A1). Thirty-eight LA-ICP-MS analyses of 54 zircon grain yielded individual $^{206}Pb/^{238}U$ dates of 423 ± 9 to 468 ± 16 Ma (Fig. 11; Table A1). Five out of six zircon grains analyzed by CA-ID-TIMS yielded a weighted mean $^{206}Pb/^{238}U$ date of 445.64 ± 0.12(0.25)[0.53] Ma interpreted to be the maximum depositional age of the rock (MSWD = 1.5, pof = 0.17; Fig. 21b; Table 1).

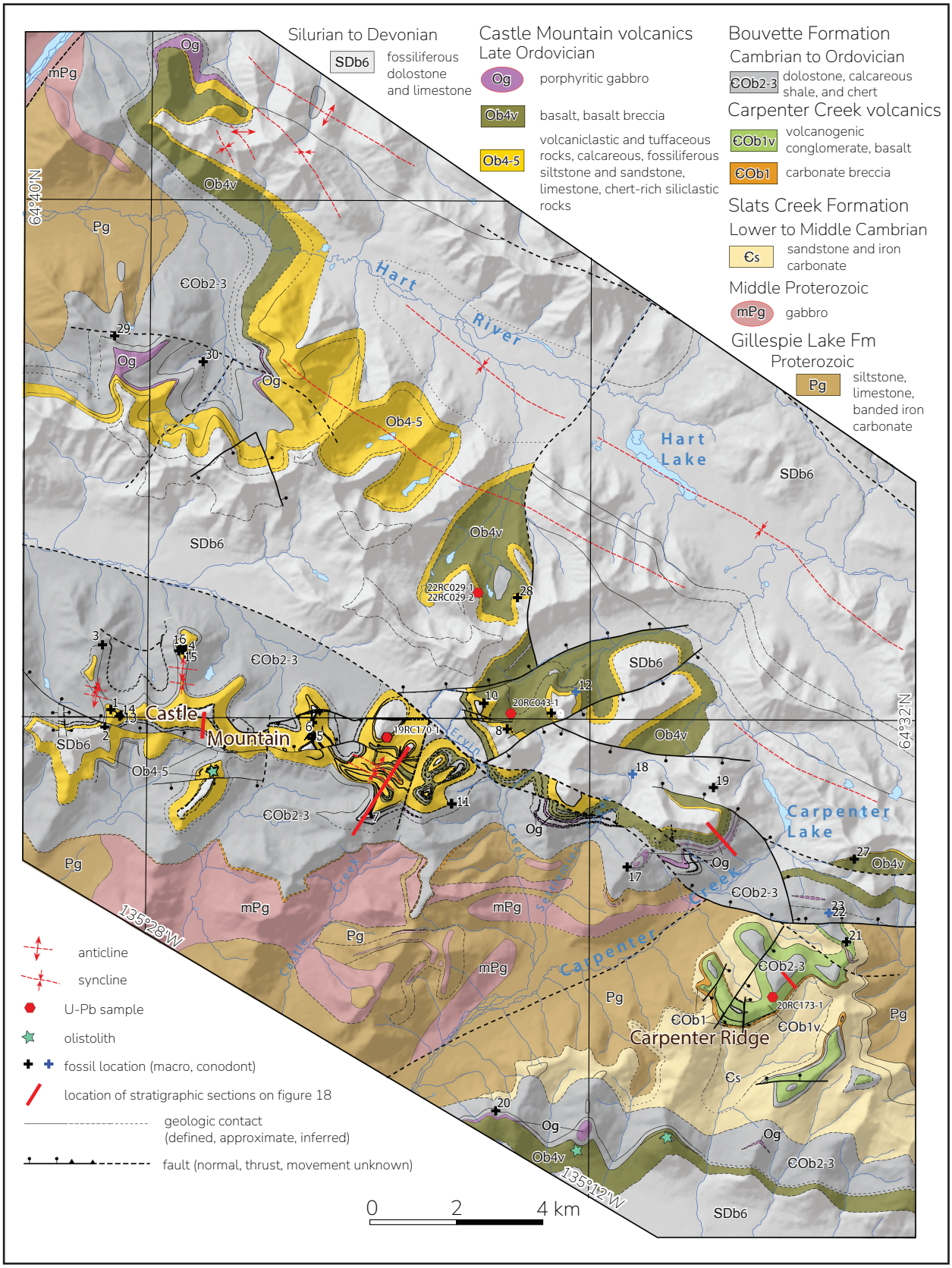

Figure 17. *Bedrock geology map of the Castle Mountain area from fault segment 3 (Yukon Geological Survey, 2024).*

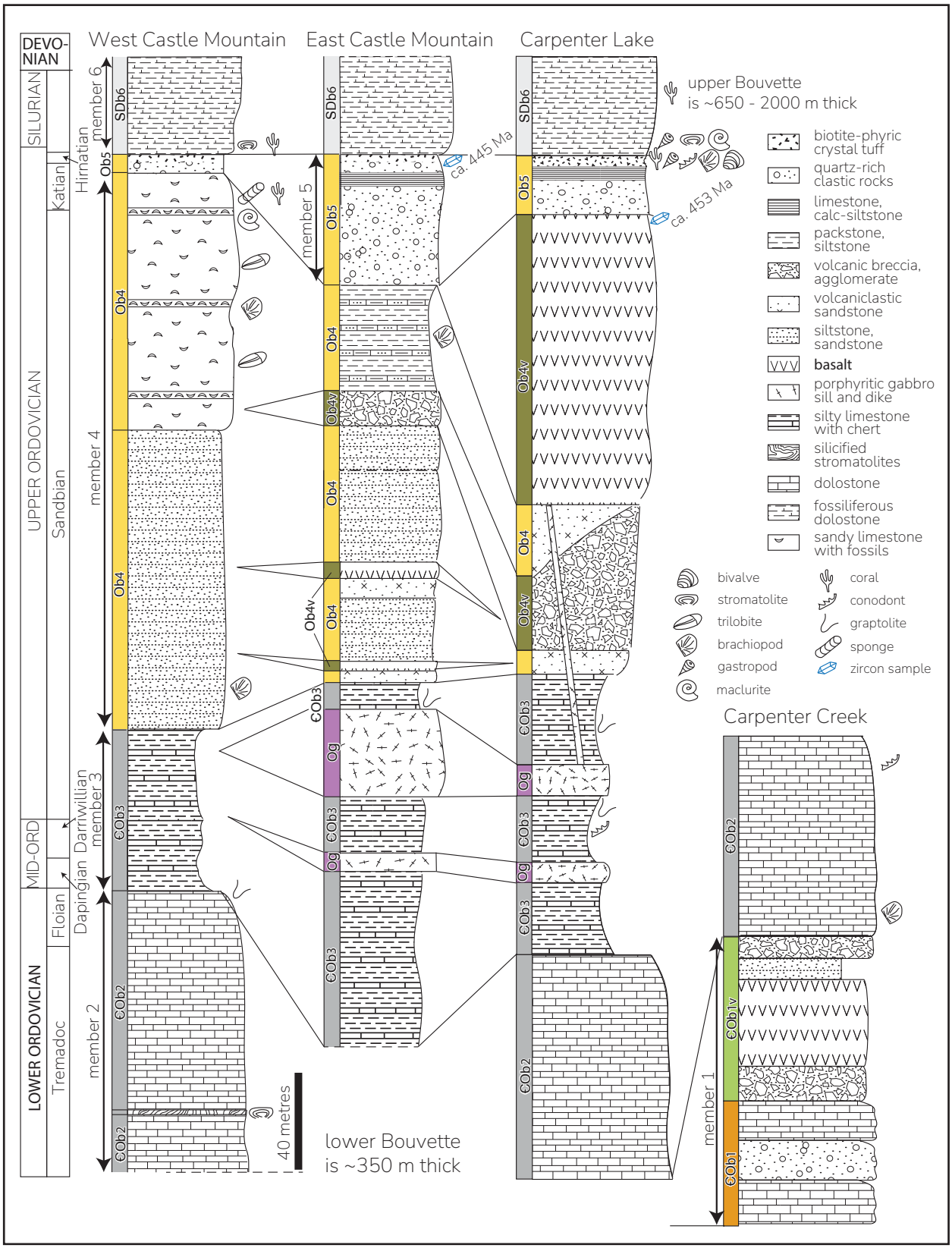

Figure 18. *Schematic stratigraphic sections from three areas across the Castle Mountain area and Carpenter Ridge (see Figure 16 for locations). Timescale is not linear and has been modified to match the thickness of the strata (Taylor et al., 2012).*

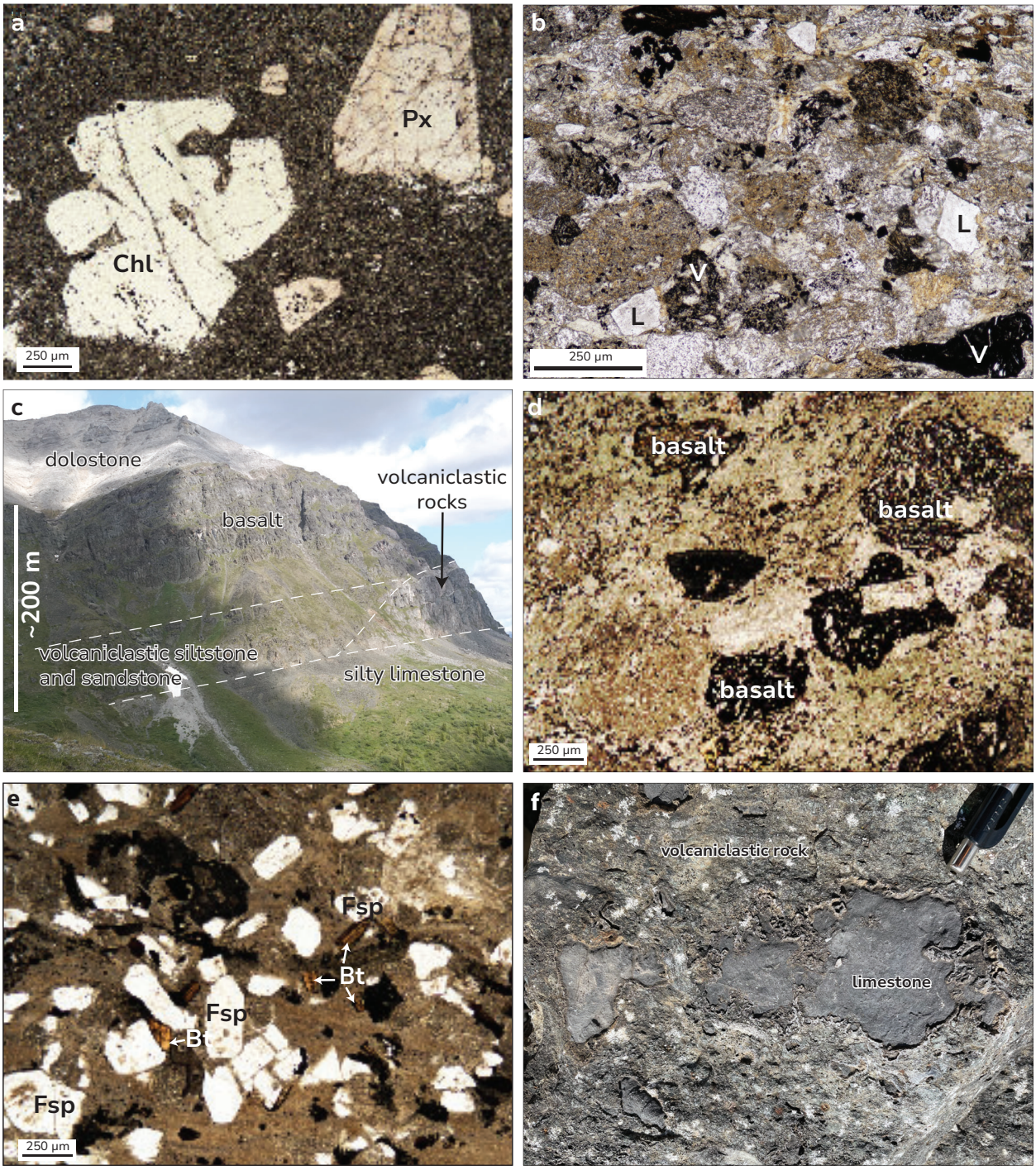

Figure 19. ***(a)*** *Thin section microphotograph of porphyritic basalt with phenocrysts of pyroxene (Px - pinkish mineral) and chlorite phenocrysts (Chl - white mineral) in an aphanitic groundmass comprised of mostly plagioclase.* ***(b)*** *Thin section microphotograph of volcaniclastic sandstone from western Castle Mountain. V- volcanic clasts, L – lithic clasts.* ***(c)*** *Looking north at volcanic rocks near Ervin Creek comprising a mound-shaped deposit of volcaniclastic rocks that laterally transitions to volcaniclastic siltstone and sandstone, and is overlain by basalt.* ***(d)*** *Volcaniclastic sandstone from a flow top near Ervin Creek. Clasts are all basalt in a chlorite-altered matrix. Zircons were collected from this sample and provide one of the U-Pb dates that constrain the eruption ages of the Castle Mountain volcanic rocks (20RC043).* ***(e)*** *Tuffaceous sandstone that contains euhedra biotite and feldspar in a muddy matrix. Fsp – feldspar, Bt - Biotite.* ***(f)*** *Irregular-shaped limestone clasts in volcaniclastic rocks from Carpenter Ridge. Some limestone clasts contain crinoid fossils.*

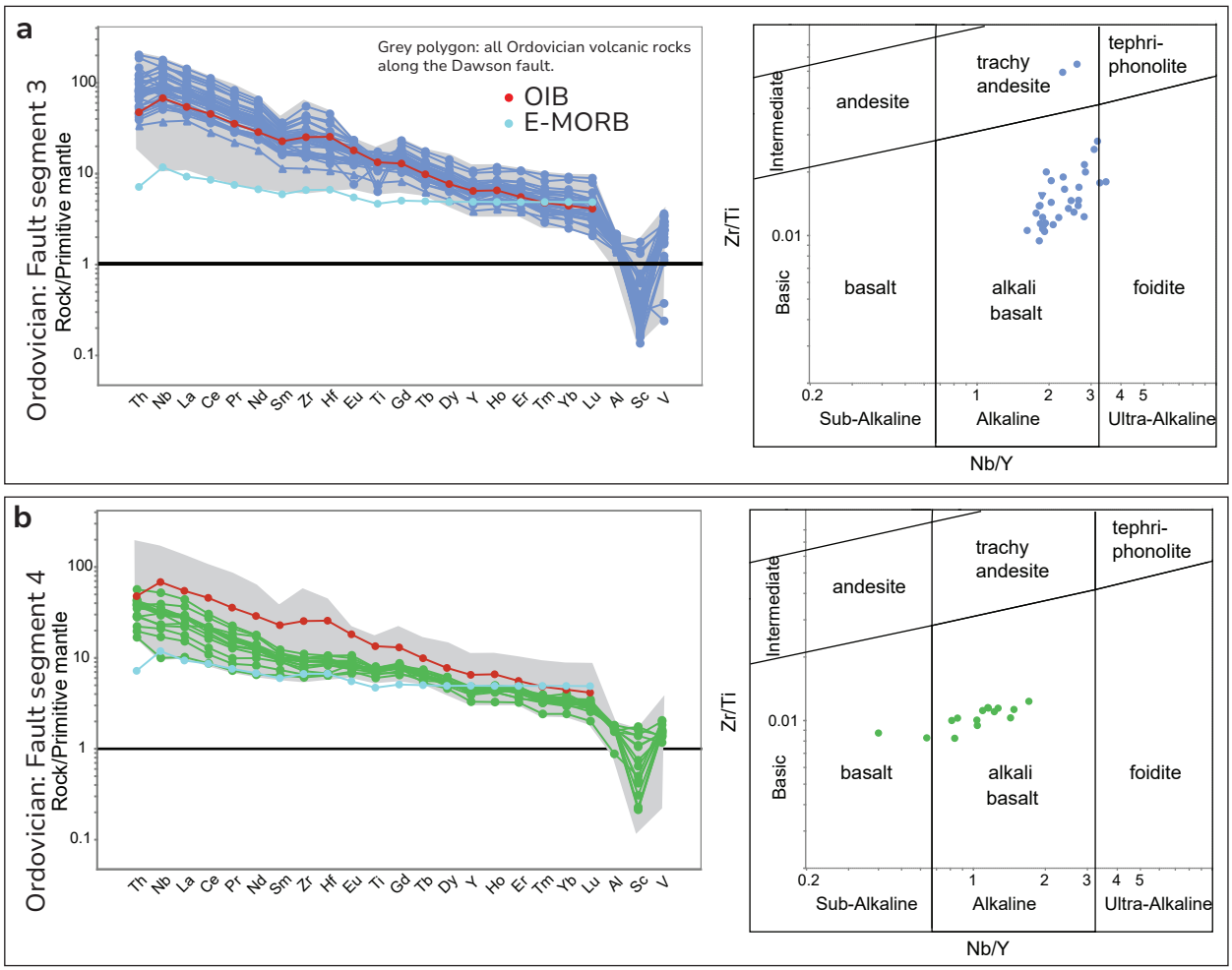

Figure 20. *Upper Ordovician volcanic rocks plotted on Zr/Ti versus Nb/Y discrimination diagram of Pearce (1996) suggesting they are predominantly alkaline to ultra-alkaline basic rocks. Upper Ordovician volcanic rocks plotted on primitive mantle normalized plots using immobile elements of Sun and McDonough (1989). Grey polygon shows the chemistry of the Upper Ordovician rocks from the Castle Mountain area.* ***(a)*** *Castle Mountain area.* ***(b)*** *Kathleen Lakes area.*

Conglomerate that contains sub-angular clasts of chert and lithics in a sandy matrix from the upper Bouvette Formation north of Hart River (22RC029-1 from Ob5; Figs. 17 and 18), yielded euhedral, oscillatory zoned, elongate zircon grains that range in size from 100 to 300 µm (Appendix A, Fig. A1). Seventy-two LA-ICP-MS analyses of 81 zircon grains yielded individual $^{206}Pb/^{238}U$ dates of 463 ± 20.1 to 413 ± 12.8 Ma (Fig. 11; Appendix A, Table A1). Four out of six zircon grains analyzed by CA-ID-TIMS yielded a weighted mean $^{206}Pb/^{238}U$ date of 446.66 ± 0.24(0.27)[0.52] Ma (MSWD = 1.0, pof = 0.40; Fig. 21c; Table 1). Two other dates agree at 447.43 ± 0.21 Ma.

Sandstone (22RC029-2 from Ob5 on; Figs. 17 and 18) with euhedral biotite and feldspar that crops out 20 to 50 m up section from sample 22RC029-1 yielded euhedral, oscillatory zoned, elongate zircon grains that range in size from 60 to 200 µm (Appendix A, Fig. A1). Fifty-five LA-ICP-MS analyses of 58 zircon grains yielded individual $^{206}Pb/^{238}U$ dates of 496 ± 18.8 to 416 ± 12.7 Ma (Fig. 11; Appendix A, Table A1). Six zircon grains analyzed by CA-ID-TIMS yielded a weighted mean $^{206}Pb/^{238}U$ date of 446.14 ± 0.13(0.18)[0.51] Ma, interpreted to be the maximum depositional age of the rock (MSWD = 0.9, pof = 0.51; Fig. 21d; Table 1).

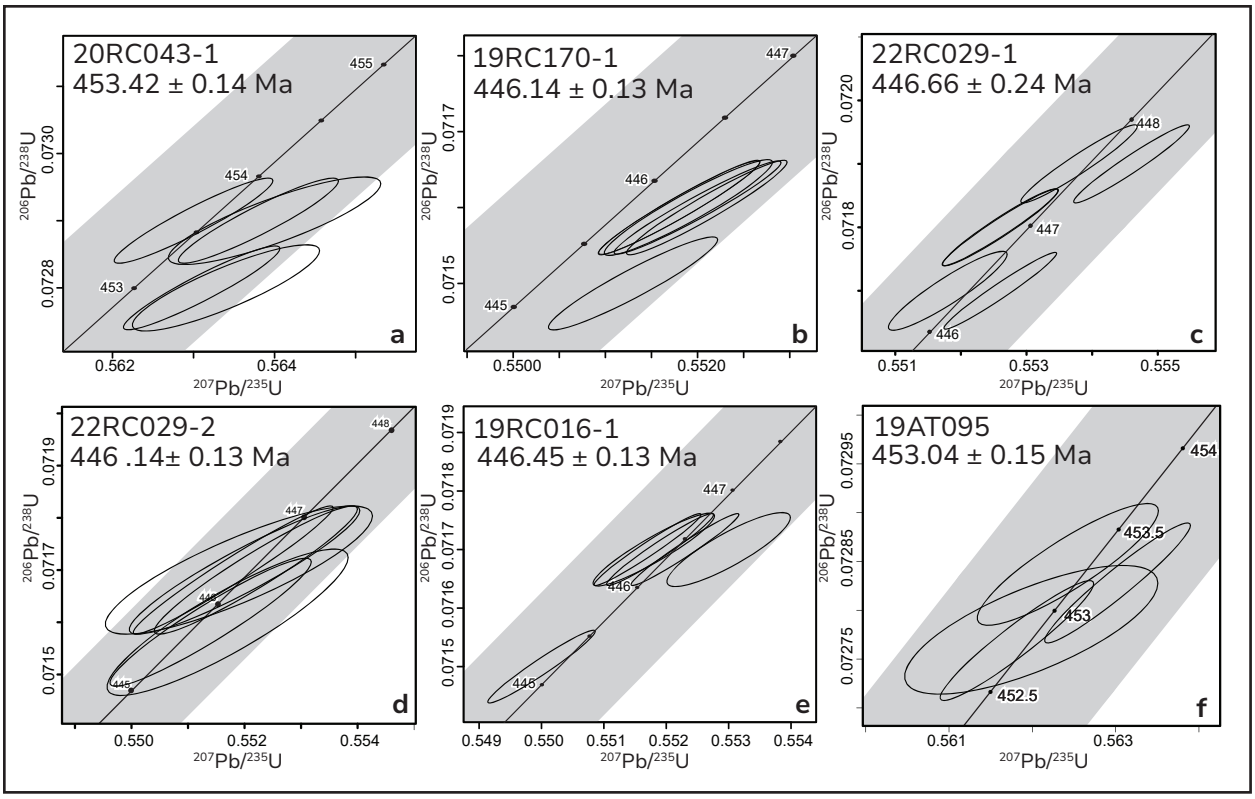

Figure 21. *Concordia plots for Upper Ordovician samples dated using CA-ID-TIMS methods.*

Kathleen Lakes area

Three intervals of basalt are interbedded with volcaniclastic and carbonate rocks of the Bouvette Formation south of Kathleen Lakes (Fig. 22). Carbonate and chlorite-altered basalt and volcaniclastic siltstone occur stratigraphically above rudstone and quartz-rich sandstone and are the lowest stratigraphic occurrence of volcanic rocks in the area. Approximately 100 m of dolomitic grainstone separates these volcanic rocks from volcanic breccia of the second interval. Locally, basalt forms 5 to 10 m wide tubes surrounded by hyaloclastite basalt cemented by calcite. Fossiliferous, silty limestone beds between this unit and the youngest volcanic interval contain crinoids, corals and trilobite fossils. The uppermost volcanic succession comprises a basal section of basalt capped by altered limestone, bioturbated limestone with coral fossils, volcanic-derived sandstone, conglomerate and fossiliferous limestone topped by a basalt flow that forms columns (Fig. 23a). Locally, within this interval, the volcanic rocks grade laterally into 50 m of volcanic-derived siltstone with distinct volcanic bombs (Fig. 23b). Dolostone with two-holed crinoids and discontinuous pods of chert-pebble conglomerate are the youngest part of the stratigraphic succession.

The volcanic rocks near Kathleen Lakes have basaltic Zr/Ti ratios of 0.008 to 0.01 (Fig. 20b). The rocks are alkaline to ultra-alkaline based on elevated Nb/Y ratios (0.4–1.7; Fig. 20b). Chromium and Ni concentrations range from 230 to 480 ppm and 113 to 256 ppm, respectively, except one sample that has Cr values over 1000 ppm and Ni values over 450 ppm (Appendix C, Table C2). These rocks have elevated TiO_2 (1.3–1.8%) relative to primitive mantle TiO_2 values (0.22%) and a range in Al_2O_3/TiO_2 ratios from 5 to 11 wt%. The P_2O_5 values range from 0.1 to 0.3 wt%. Compared to the primitive mantle, the volcanic rocks from this area have strong LREE enrichment (La_{pm}/Sm_{pm} = 1.6 to 3.6) and HREE depletion compared to MREE

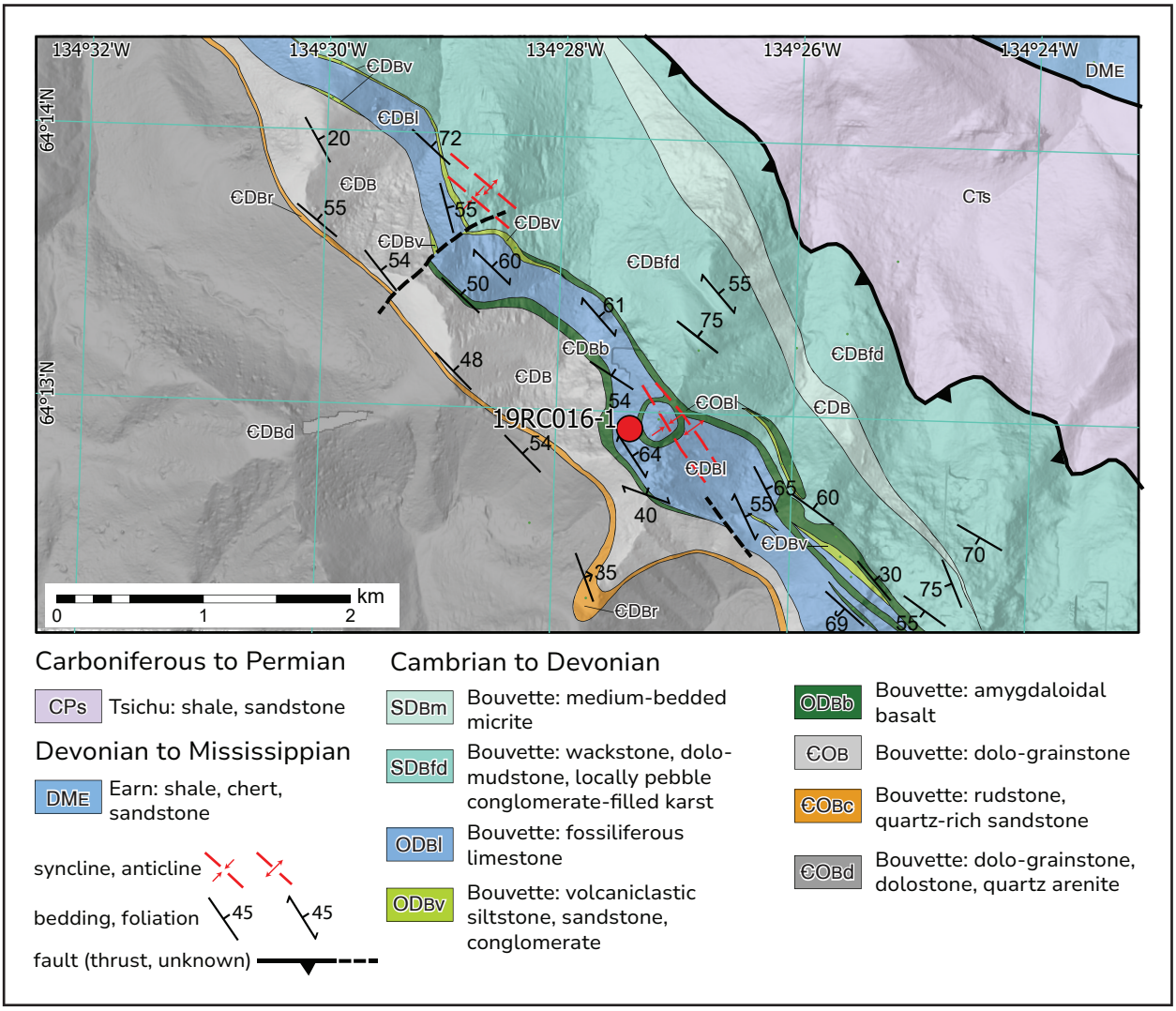

Figure 22. *Bedrock geology map of the Kathleen Lakes area from fault segment 3 (Yukon Geological Survey, 2024).*

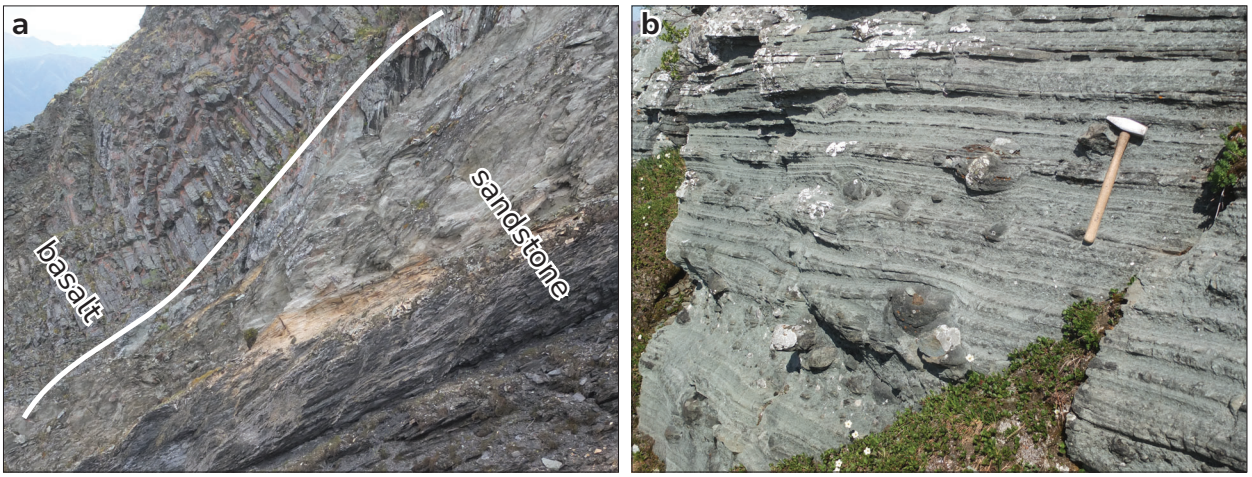

Figure 23. (a) *Sheared maroon sandstone and limestone in contact with basalt that forms columns. The basalt in this photo transitions to siltstone and sandstone displayed in (b) of this figure.* ***(b)*** *Sandstone and siltstone with volcanic bombs.*

(Sm_{pm}/Yb_{pm} = 2.2 to 4.7; Fig. 20b).

A bed of calcareous sandstone with angular to sub-angular grains of vitreous quartz, feldspar and dark lithic clasts occurs directly above basalt and below volcaniclastic conglomerate (Fig. 22). Zircon crystals from this bed (19RC016-1) range in size from 125 to 250 µm, are dominantly equant with both oscillatory and sector zoning (Appendix A, Fig. A1). Zircon grains (n = 110) from this sample yielded individual $^{206}Pb/^{238}U$ LA-ICP-MS dates of 420 ± 7 to 456 ± 11 Ma and two zircon grains that yielded individual $^{206}Pb/^{238}U$ LA-ICP-MS dates of 2646 ± 42 and 2306 ± 42 Ma (Fig. 11; Appendix A, Table A1). Five of six grains from the younger group of zircons were analyzed by CA-ID-TIMS and yielded a weighted mean $^{206}Pb/^{238}U$ date of 446.36 ± 0.19(0.23)[0.53] interpreted to be the crystallization age of the volcanic rocks in this area (MSWD = 2.1, pof = 0.08; Fig. 21e; Table 1).

East of Kathleen Lakes, a volcaniclastic sandstone that occurs within the middle of the Bouvette Formation (Fig. 24) carbonate yielded twenty-two zircon grains with individual $^{206}Pb/^{238}U$ LA-ICP-MS dates of 454 ± 11 to 506 ± 13 Ma and two other individual dates of 1101 ± 32 and 1110 ± 29 Ma (19TA095; Fig. 11; Appendix A, Table A1). Eight of the youngest grains were analyzed by CA-ID-TIMS, four of which yielded a weighted mean date of 453 ± 0.15(0.27)[0.54] interpreted to be the age of the eruption (MSWD = 2.1, pof = 0.09; Fig. 21f; Table 1).

Petrogenesis of the Upper Ordovician volcanic rocks

Small-volume alkali basalts are common in continental rifts and continental arc rifts (e.g., Goodfellow et al., 1995; Shinjo et al., 1999; van Staal et al., 1991) and their geochemical compositions indirectly constrain the depth and degree of partial melting, mantle sources

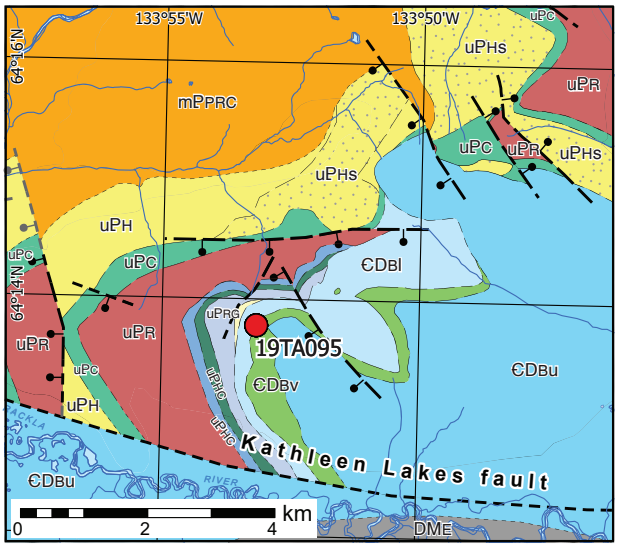

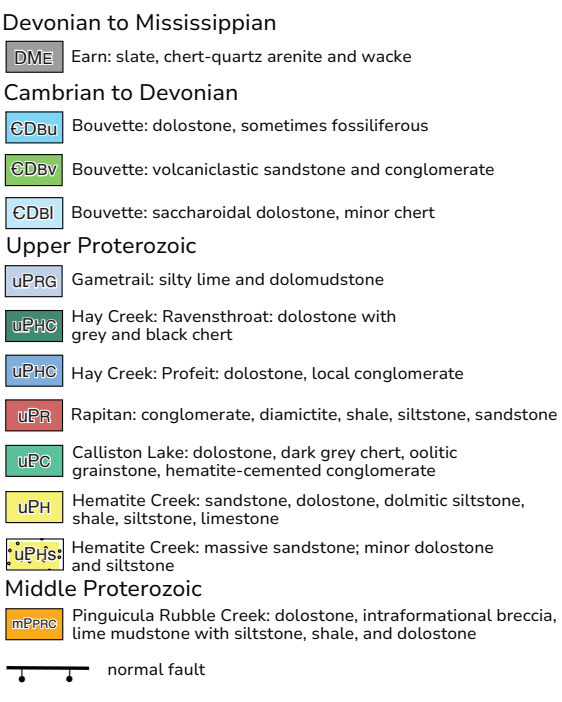

Figure 24. *Bedrock geology east of Kathleen Lakes along Dawson fault segment 4 (Ambrose and Bowie, 2020).*

and how magma batches are modified during transport to the Earth's surface. Whole-rock major and trace element concentrations and Nd-Hf isotope geochemical compositions provide insights into petrogenetic conditions of formation globally (e.g., Batiza and Vanko, 1984; Beard and Johnson, 1993; Fitton and Dunlop, 1985; Pe-Piper et al., 1994), including studies of lower Paleozoic mafic rocks in central Yukon (Goodfellow et al., 1995; Campbell et al., 2019; Cobbett et al., 2023).

Lower and middle Paleozoic strata were metamorphosed to lower greenschist facies during Mesozoic regional deformation (Read et al., 1991), necessitating selective sampling to obtain the least altered rocks. Typical alteration features include mafic minerals partly replaced by chlorite and calcite. Amygdules are filled with quartz and calcite, and quartz occurs as alteration rims on some phenocrysts. Major elements (except Al_2O_3, TiO_2, P_2O_5) and LFSE: (Ba, Sr, Cs, Rb) are considered mobile during greenschist facies metamorphism and seafloor alteration, and the interpretations presented are thus based on immobile element systematics (Whitford et al., 1989; MacLean, 1990). Rare earth elements, HFSE, transition elements, and Th are considered immobile under the metamorphic and alteration conditions experienced by the sampled rocks (Lesher et al., 1986; MacLean, 1990; Jenner, 1996). Each immobile element and element ratio was plotted against the Al_2O_3/Na_2O alteration index to test immobility and to demonstrate that key petrological elements and ratios used below were not affected by alteration and metamorphism and reflect primary igneous compositions of the rocks (Spitz and Darling, 1978; Piercey et al., 2002; see Appendix A, Fig. A2).

The Upper Ordovician igneous rocks (including Castle Mountain volcanics and volcanic rocks near Kathleen Lakes) are dominantly alkali basalt (Fig. 20). Castle Mountain volcanic rocks have ocean island basalt-like trace element patterns. Some samples have a relatively smooth pattern on primitive mantle normalized multi-element plots (i.e., there are no positive Zr-Hf anomalies), while others have positive Zr/Hf anomalies compared to Sm. The volcanic rocks near Kathleen Lakes have trace element patterns between ocean island basalt and enriched mid-ocean ridge basalt (Figs. 20).

The primitive mantle-normalized multi-element patterns of the Castle Mountain volcanics and the volcanic rocks near Kathleen Lakes are consistent with low degree partial melting of an enriched source at >75 km depth (Fig. 25a; e.g., Kay and Gast, 1973; Pearce, 2008, 2014; Rogers, 2015; Ellam, 1992; Roex et al., 2001). Highly incompatible elements such as LREE become enriched in the melt during low-degree partial melting of LREE enriched sources (e.g., Kay and Gast, 1973; Rogers, 2015). If the melts are not subsequently diluted by higher volume melting (like at a mid-ocean ridge), the result is a volcanic suite that only contains alkaline rocks like the Castle Mountains volcanics. At these depths, garnet is stable and will retain HREE during partial melting resulting in HREE depleted alkaline rocks and coincident LREE enrichment relative to HREE (Fig. 25a; Ellam, 1992). Partial melts of the subcontinental lithospheric mantle have ocean island basalt-like geochemical compositions because of earlier metasomatism (e.g., Hawkesworth et al., 1990; Gallagher and Hawkesworth, 1992; Roex et al., 2001) and are a likely source for the Upper Ordovician volcanic rocks along the Dawson fault.

There are variations in the Zr/Hf-Sm systematics of the Upper Ordovician volcanic rocks despite derivation from garnet-bearing lithospheric sources. Notably, some samples have high Zr/Hf-Sm ratios, which suggests that these melts not only had garnet, but also had amphibole as a restite phase, or that amphibole fractionally crystallized, as amphibole preferentially retains Sm over Zr and Hf (Fig. 20; e.g., Foley et al., 2002). Samples with or without Zr/Hf-Sm anomalies from the Castle Mountain volcanics occur throughout the volcanic succession, suggesting amphibole

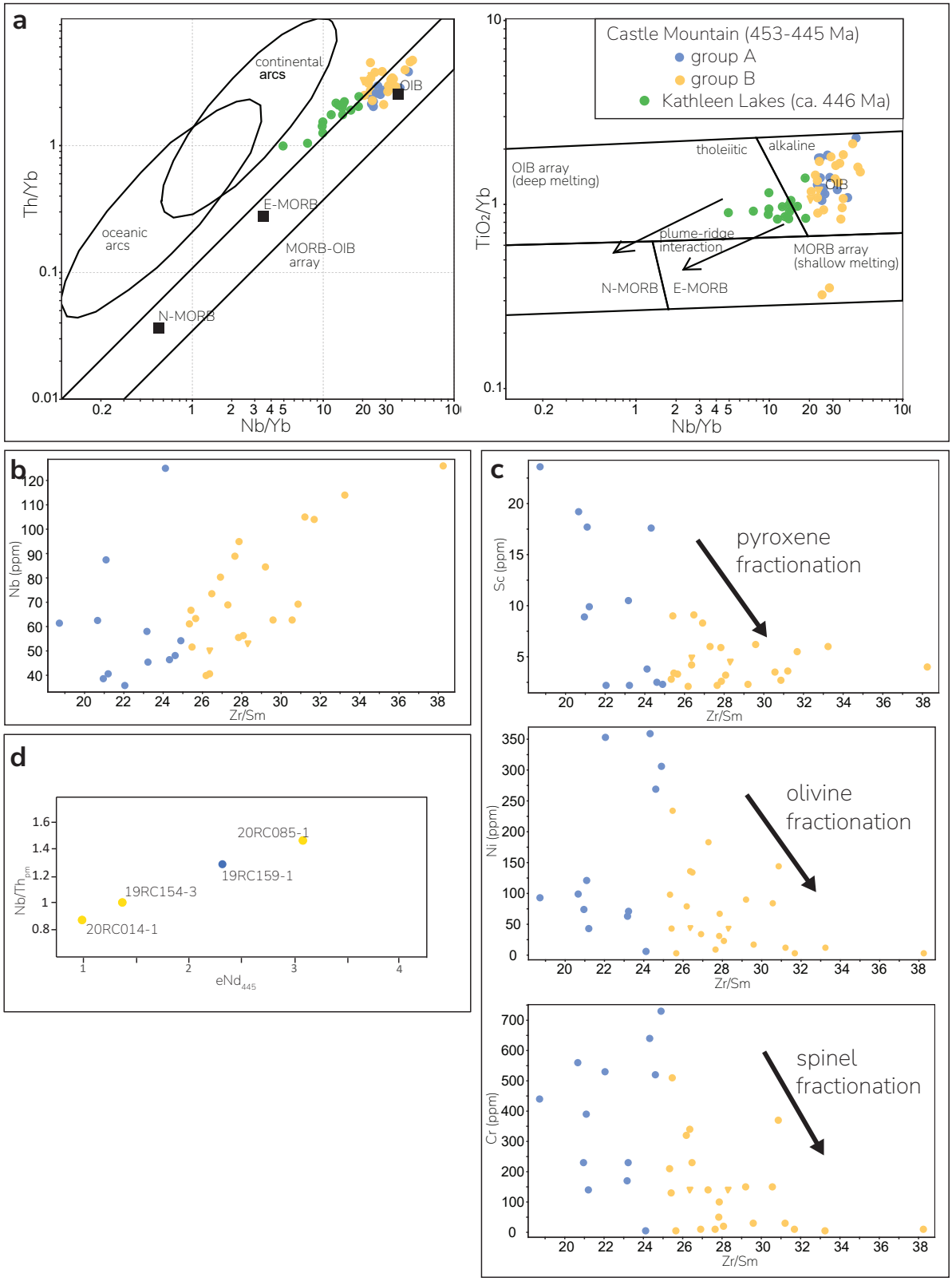

Figure 25. *Geochemical discrimination diagrams of Upper Ordovician volcanic rocks.* ***(a)*** *Th/Yb versus Nb/Yb of Pearce (2008) showing Castle Mountain volcanics plotting along the edge of the mantle array near OIB. Kathleen Lakes volcanic rocks occur outside the mantle array between E-MORB and OIB. Diagram on the right plots TiO_2/Yb versus Nb/Yb and suggests the Upper Ordovician volcanic rocks formed from deep mantle melting.* ***(b)*** *Incompatible element Nb versus Zr/Sm displaying a positive correlation.* ***(c)*** *Compatible elements, Sc, Ni, and Cr, versus Zr/Sm displaying a negative correlation.* ***(d)*** *Primitive mantle normalized Nb/Th and Nb/La versus epsilon Nd_{445}.*

was likely not a resite phase. Instead, variable fractionation of amphibole may better explain the Zr/Hf-Sm anomalies. To test this idea, Zr/Sm is plotted against both incompatible (e.g., Nb) and compatible (e.g., Sc, Ni, Cr) elements (Fig. 25b-c). Samarium, along with compatible elements that preferentially incorporate into mafic minerals, such as olivine and pyroxene, are removed from the melt preferentially over Zr and Hf when amphibole fractionates. The removal of these elements during fractional crystallization would facilitate the concentration of incompatible elements such as Nb and result in positive correlations between the ratio Zr/Sm (i.e., increases with fractionation) and incompatible elements (Fig. 25b), and a negative correlation between incompatible elements (Fig. 25c). Thus, fractionation of amphibole and other mafic phases best explains the Zr/Hf-Sm anomalies of the Castle Mountain volcanic rocks.

Castle Mountain volcanics have flat to positive Th-Nb-La primitive mantle normalized patterns and low $^{143}Nd/^{144}Nd$ and $^{176}Hf/^{177}Hf$ ratios with εNd_{445} values = +1 to +3 and εHf_{445} = +1 to +4. The latter eNd_{445} and eHf_{445} values are lower than the depleted mantle at 445 Ma (εNd_{DMt} = 9.4, εHf_{DMt} = 14), which reflect crustal contamination or melting part of the mantle that evolved towards low εNd and εHf as a result of LREE-enrichment (e.g., Piercey et al., 2006). In Figure 25d, εNd is plotted against primitive mantle-normalized Nb/Th with a positive correlation, suggesting that the isotopic values of the Castle Mountain rocks are a result of crustal contamination (e.g., Pearce and Peate, 1995; Pearce, 2008; Piercey et al., 2006, 2012).

Summary

Upper Cambrian to Upper Ordovician mafic volcanic and volcaniclastic rocks and gabbro occur in the vicinity of the surface trace of the Dawson fault in the Yukon. Precise ages of eruption and crystallization ages of the volcanic rocks have been determined through U-Pb zircon CA-ID-TIMS analyses and indicate magmatism occurred in two pulses along the Dawson fault ca. 501–497 and 453–445 Ma. Fossil age constraints from sedimentary rocks that are interbedded with, or enclose the volcanic stratigraphy, agree with the U-Pb dates. These rocks are predominantly alkali basalt and have ocean island basalt like trace element geochemical compositions consistent with low degree partial melting of an enriched source such as the metasomatized sub-continental lithospheric mantle. The HREE depletion suggests the melts formed from the garnet stability field. The fractionation of amphibole and other mafic phases explains the trace element patterns of the Castle Mountain volcanic rocks. Initial εHf and εNd values of the volcanic rocks range from +0.7 to +8.5 and +0.5 to +3.8, respectively. A more in-depth interpretation of the tectonic significance of igneous rocks along the Dawson fault is presented in Cobbett et al. (2025).

References

Abbott, J.G., 1997. Geology of the Upper Hart River area, Eastern Ogilvie Mountains, Yukon Territory (116A/10, 116A/11). Exploration and Geological Services Division, Yukon, Indian and Northern Affairs Canada, Bulletin 9, 92 p.

Ambrose, T., 2021. Update on the bedrock geology of the Rusty Mountain area, southern Wernecke Mountains, Yukon (parts of NTS 106C/4, 5, 12 and 106D/1, 8). In: Yukon Exploration and Geology 2020, K.E. MacFarlane (ed.), Yukon Geological Survey, p. 95-113.

Ambrose, T., 2022. Update on the bedrock geology of the Rusty Mountain and Bonnet Plume Pass (west half) areas. In: Yukon Exploration and Geology 2021, K.E. MacFarlane (ed.), Yukon Geological Survey, p. 13-36.

Ambrose, T. and Bowie, S., 2020. Preliminary report on the bedrock geology of the Rackla River area, southern Wernecke Mountains, Yukon (parts of NTS 106C/4, 5 and 106D/1, 8). In: Yukon Exploration and Geology 2019, K.E. MacFarlane (ed.), Yukon Geological Survey, p. 1-21.

Batiza, R. and Vanko, D., 1984. Petrology of young Pacific seamounts. Journal of Geophysical Research: Solid Earth, vol. 89, no. B13, p. 11235-11260.

Beard, B. L. and Johnson, C. M., 1993. Hf isotope composition of late Cenozoic basaltic rocks from northwestern Colorado, USA: New constraints on mantle enrichment processes. Earth and Planetary Science Letters, vol. 119, no. 4, p. 495-509.

Blichert-Toft, J., and Albarède, F., 1997. The Lu-Hf isotope geochemistry of chondrites and the evolution of the mantle-crust system. Earth and Planetary Science Letters, vol. 148, no. 1-2, p. 243-258.

Bouvier, A., Vervoort, J.D., and Patchett, P.J., 2008. The Lu–Hf and Sm–Nd isotopic composition of CHUR: constraints from unequilibrated chondrites and implications for the bulk composition of terrestrial planets. Earth and Planetary Science Letters, vol. 273, no. 1-2, p. 48-57.

Busch, J.F., Strauss, J.V., Saylor, M.H., Allen, T.J., Faehnrich, K. and Taylor, J.F. 2019. Preliminary observations of the Bouvette Formation at Nadaleen Mountain, Yukon (NTS 106C/2, 3). In: Yukon Exploration and Geology 2019, K.E. MacFarlane (ed.). Yukon Geological Survey, p. 19-42.

Campbell, R.W., Beranek, L.P., Piercey, S.J. and Friedman, R., 2019. Early Paleozoic post breakup magmatism along the Cordilleran margin of western North America: New zircon U-Pb age and whole-rock Nd-and Hf-isotope and lithogeochemical results from the Kechika group, Yukon, Canada. Geosphere, vol. 15, 29 p., https://doi.org/10.1130/GES02044.1.

Cecile, M., Morrow, D. and Williams, G., 1997. Early Paleozoic (Cambrian to Early Devonian) tectonic framework, Canadian Cordillera. Bulletin of Canadian Petroleum Geology, vol. 45, no. 1, p. 54-74.

Cobbett, R., 2020. Preliminary report on the bedrock geology of Castle Mountain area, Yukon (parts of NTS 105D/6). In: Yukon Exploration and Geology 2019, K.E. MacFarlane (ed.), Yukon Geological Survey, p. 43–55.

Cobbett, R.N., 2022. Geology of the Carpenter Creek and McKay Hill areas (NTS 106D/6, 11), central Yukon. Yukon Exploration and Geology 2021, K.E. MacFarlane (ed.), Yukon Geological Survey, p. 125-142.

Cobbett, R.N., Beranek, L.P., Piercey, S.J., Crowley, J.L. and Colpron, M., 2023. Early Ordovician seamounts preserved in the Canadian Cordillera: Implications for the rift history of western Laurentia. Geosphere, vol. 19, no. 5, p. 1421-1451, https://doi.org/10.1130/GES02613.1.

Cobbett, R.N., Beranek, L.P., Colpron, M., Piercey, S., Crowley, J.L., Strauss, J.V. and Taylor, J.F., 2025. Late Cambrian and Ordovician alkalic magmatism along the Dawson fault, Yukon: Evidence for multiple reactivations of a rift-transfer fault in the northern Canadian Cordillera. Tectonics, vol. 44, no. 2, e2024TC008645, https://doi.org/10.1029/2024TC008645.

Colpron, M., 2012. Preliminary observations on the geology of the Rackla belt, Mount Ferrell map area (NTS 106C/3), central Yukon. In: Yukon Exploration and Geology 2011, K.E. MacFarlane and P.J. Sack (eds.), Yukon Geological Survey, p. 27-43.

Colpron, M., Moynihan, D., Israel, S. and Abbott, G., 2013. Geological map of the Rackla belt, east-central Yukon (NTS 106C/1-4, 106D/1). Yukon Geological Survey, 1:50 000 scale, 5 maps and legend.

Connelly, J., Ulfbeck, D., Thrane, K., Bizzarro, M. and Housh, T., 2006. A method for purifying Lu and Hf for analyses by MC-ICP-MS using TODGA resin. Chemical Geology, vol. 233, no. 1-2, p. 126-136.

Crowley, J.L., Schoene, B. and Bowring, S.A., 2007. U-Pb dating of zircon in the Bishop Tuff at the millennial scale. Geology, vol. 35, no. 5, p. 1123-1126.

Ellam, R., 1992. Lithospheric thickness as a control on basalt geochemistry. Geology, vol. 20, no. 2, p. 153-156.

Evans, K.V. and Clemons, R.E., 1988. Cambrian-Ordovician (500 Ma) alkalic plutonism in southwestern New Mexico; U-Th-Pb isotopic data from the Florida Mountains. American Journal of Science, vol. 288, no. 7, p. 735-755.

Evans, K.V. and Zartman, R.E., 1988. Early Paleozoic alkalic plutonism in east-central Idaho. Geological Society of America Bulletin, vol. 100, no. 12, p. 1981-1987.

Eyster, A., Ferri, F., Schmitz, M.D. and Macdonald, F.A., 2018. One diamictite and two rifts: Stratigraphy and geochronology of the Gataga Mountain of northern British Columbia. American Journal of Science, vol. 318, no. 2, p. 167-207.

Fitton, J. and Dunlop, H., 1985. The Cameroon line, West Africa, and its bearing on the origin of oceanic and continental alkali basalt. Earth and Planetary Science Letters, vol. 72, no. 1, p. 23-38.

Foley, S., Tiepolo, M. and Vannucci, R., 2002. Growth of early continental crust controlled by melting of amphibolite in subduction zones. Nature, vol. 417, no. 6891, p. 837-840.

Gabrielse, H., Blusson S.L. and Roddick J., 1973. Geology of Flat River, Glacier Lake, and Wrigley Lake Map-areas, District of Mackenzie and Yukon Territory: General Geology, Structural Geology and Economic Geography, Department of Energy, Mines and Resources, Memoir 366, 153 p.

Gallagher, K. and Hawkesworth, C., 1992. Dehydration melting and the generation of continental flood basalts. Nature, vol. 358, no. 6381, p. 57-59.

Gerstenberger, H. and Haase, G., 1997. A highly effective emitter substance for mass spectrometric Pb isotope ratio determinations. Chemical Geology, vol. 136, no. 3-4, p. 309-312.

Goodfellow, W.D., Cecile, M.P. and Leybourne, M.I., 1995. Geochemistry, petrogenesis, and tectonic setting of lower Paleozoic alkalic and potassic volcanic rocks, Northern Canadian Cordillera Miogeocline. Canadian Journal of Earth Sciences, vol. 32, p. 1236-1254.

Green, L.H., 1972. Geology of Nash Creek, Larsen Creek, and Dawson Map-Areas, Yukon Territory. Geological Survey of Canada, Memoir 364, 157 p.

Hawkesworth, C., Kempton, P., Rogers, N., Ellam, R. and Van Calsteren, P., 1990. Continental mantle lithosphere, and shallow level enrichment processes. Earth and Planetary Science Letters, vol. 96, p. 256-268.

Hiess, J., Condon, D.J., McLean, N. and Noble, S. R., 2012. $^{238}U/^{235}U$ systematics in terrestrial uranium-bearing minerals. Science vol. 335, no. 6067, p. 1610-1614.

Jacobsen, S.B. and Wasserburg, G.J., 1980. Sm-Nd isotopic evolution of chondrites. Earth and Planetary Science Letters, vol. 50, no. 1, p. 139-155.

Jaffey, A.H., Flynn, K.F., Glendenin, L.E., Bentley, W.C. and Essling, A.M., 1971. Precision measurements of half-lives and specific activities of 235U and 238U. Physical Review, vol. C4, no. 5, p. 1889-1906.

Jenner, G.A., 1996. Trace element geochemistry of igneous rocks: geochemical nomenclature and analytical geochemistry. In: Trace element geochemistry of volcanic rocks: applications for massive sulfide exploration, Wyman, D.A., (ed.). Geological Association of Canada, short course notes, vol. 12, p. 51-77.

Kay, R. W. and Gast, P. W., 1973. The Rare Earth Content and Origin of Alkali-Rich Basalts. The Journal of Geology, vol. 81, no. 6, p. 653-682.

Krogh, T.E., 1973. A low contamination method for hydrothermal decomposition of zircon and extraction of U and Pb for isotopic age determination. Geochimica et Cosmochimica Acta, vol. 37, no. 3, p. 485-494.

Kuiper, Y.D., Murray, D.P., Ellison, S. and Crowley, J.L., 2022. U-Pb detrital zircon analysis of sedimentary rocks of the southeastern New England Avalon terrane in the U.S. Appalachians. Evidence for a separate crustal block. New Developments in the Appalachian-Caledonian-Variscan Orogen. Geological Society of America Northeastern Section-56th Annual Meeting-2021 Conference Paper, https://doi.org/10.1130/SPE554.

Lesher, C., Gibson, H. and Campbell, I., 1986. Composition-volume changes during hydrothermal alteration of andesite at Buttercup Hill, Noranda District, Quebec. Gochimica et Cosmochimica Acta, vol. 50, no. 12, p. 2693-2705.

Leslie, C.D., 2009. Detrital zircon geochronology and rift-related magmatism: central Mackenzie Mountains, Northwest Territories. Unpublished MSc thesis, University of British Columbia, British Columbia, Canada, 224 p.

Li, Z.-X., Bogdanova, S., Collins, A., Davidson, A., De Waele, B., Ernst, R., Fitzsimons, I., Fuck, R., Gladkochub, D. and Jacobs, J., 2008. Assembly, configuration, and break-up history of Rodinia: a synthesis. Precambrian research, vol. 160, no. 1-2, p. 179-210.

Ludwig, K.R., 2003. User's Manual for Isoplot 3.00. Berkeley Geochronology Center. Berkeley, California, 70 p.

Lund, K., 2008. Geometry of the Neoproterozoic and Paleozoic rift margin of western Laurentia: Implications for mineral deposit settings. Geosphere, vol. 4, no. 2, p. 429-444.

Lund, K., Aleinikoff, J., Evans, K., DuBray, E., Dewitt, E. and Unruh, D., 2010. SHRIMP U-Pb dating of recurrent Cryogenian and Late Cambrian–Early Ordovician alkalic magmatism in central Idaho: Implications for Rodinian rift tectonics. Geological Society of America Bulletin, vol. 122, no. 3-4, p. 430-453.

MacLean, W., 1990. Mass change calculations in altered rock series. Mineralium Deposita, vol. 25, no. 1, p. 44-49.

MacNaughton, R.B., Moynihan, D.P., Roots, C.F. and Crowley, J.L., 2016. New occurrences of Oldhamia in eastern Yukon, Canada: Stratigraphic context and implications for Cambrian deep-marine biostratigraphy. Ichnos, vol. 23, no. 1-2, p. 33-52.

Madronich, L.I., 2019. Detrital zircon U-Pb ages and trace element compositions from Cambrian rocks of western North America, Unpublished MSc thesis, University of Calgary. Alberta, Canada, 125 p.

Mamrol, P., 2016. New geochronological and geochemical constraints on volcanic rocks from the Ogilvie Mountains, west-central Yukon, Canada. Unpublished undergraduate Senior Thesis, Dartmouth College, Hanover, New Hampshire, 68 p.

Mattinson, J.M., 2005. Zircon U-Pb chemical abrasion ("CA-TIMS") method: combined annealing and multi-step partial dissolution analysis for improved precision and accuracy of zircon ages. Chemical Geology, vol. 220, no. 1-2, p.47-66.

Morrow, D.W., 1999. Lower Paleozoic stratigraphy of northern Yukon Territory and northwestern District of Mackenzie. Geological Survey of Canada, Bulletin 538, 202 p.

Moynihan, D., 2014. Bedrock Geology of NTS 106B/04, Eastern Rackla Belt. In: Yukon Exploration and Geology 2013, K.E. MacFarlane, M.G. Nordling, and P.J. Sack (eds.), Yukon Geological Survey, p. 147-167.

Moynihan, D., 2016. Bedrock Compilation of the eastern Rackla belt, NTS 105N/15, 105N/16,105O/13, 106N/04, 106C/01, 106C/02, east-central Yukon. Yukon Geological Survey, Open File 2016-2, scale 1:75 000, 2 sheets.

Pe-Piper, G., Jansa, L. and Palacz, Z., 1994. Geochemistry and regional significance of the Early Cretaceous bimodal basalt-felsic associations on Grand Banks, eastern Canada. Geological Society of America Bulletin, vol. 106, no. 10, p. 1319-1331.

Pearce, J.A., 1996. A user's guide to basalt discrimination diagrams. In: Trace element geochemistry of volcanic rocks: Applications for massive sulphide exploration, D. A. Wyman (Ed.), Geological Association of Canada, Short Course Notes, vol. 12, pp. 79-113.

Pearce, J.A., 2008. Geochemical fingerprinting of oceanic basalts with applications to ophiolite classification and the search for Archean oceanic crust. Lithos, vol. 100, no. 1-4, p. 14-48.

Pearce, J.A., 2014. Immobile element fingerprinting of ophiolites. Elements, vol. 10, no. 2, p. 101-108.

Pearce, J.A. and Peate, D.W., 1995. Tectonic implications of the composition of volcanic arc magmas. Annual Reviews of Earth and Planetary Science, vol. 23, p. 251-285.

Piercey, S J., Mortensen, J.K., Murphy, D.C., Paradis, S. and Creaser, R.A., 2002. Geochemistry and tectonic significance of alkalic mafic magmatism in the Yukon-Tanana Terrane, Finlayson Lake Region, Yukon. Canadian Journal of Earth Sciences, vol. 39, p. 1729-1744.

Piercey, S.J., Murphy, D.C. and Creaser, R.A., 2012. Lithosphere-asthenosphere mixing in a transform-dominated late Paleozoic backarc basin: Implications for northern Cordilleran crustal growth and assembly. Geosphere, vol. 8, no. 3, p. 716-739.

Piercey, S.J., Nelson, J L., Colpron, M., Dusel-Bacon, C., Simard, R.-L. and Roots, C.F., 2006. Paleozoic magmatism and crustal recycling along the ancient Pacific margin of North America, northern Cordillera: Paleozoic evolution and metallogeny of pericratonic terranes at the ancient Pacific margin of North America, Canadian and Alaskan Cordillera. Geological Association of Canada Special Paper 45, p. 281-322.

Pigage, L., Crowley, J., Pyle, L., Abbott, J., Roots, C. and Schmitz, M., 2012. U–Pb zircon age of an Ordovician tuff in southeast Yukon: Implications for the age of the Cambrian–Ordovician boundary. Canadian Journal of Earth Sciences, vol. 49, no. 6, p. 732-741.

Pigage, L., Roots, C. and Abbott, J., 2015. Regional bedrock geology for Coal River map area (NTS 95D), southeast Yukon. Yukon Geological Survey, Bulletin 17, 155 p.

Pratt, B.R., 1991. Trilobites of the Marjuman and Steptoean stages (Upper Cambrian), Rabbitkettle Formation, Southern Mackenzie Mountains, northwest Canada. Paleontographica Canadiana, vol. 9, 179 p.

Rasetti, F., 1966. New Lower Cambrian trilobite fauna from the Taconic sequence of New York. Smithsonian Institution, vol. 148, no. 1-9, 48 p.

Read, P.B., Woodsworth, G.J., Greenwood, H.J., Ghent, E.D. and Evenchick, C. A., 1991. Metamorphic map of the Canadian Cordillera. Geological Survey of Canada, scale 1:2 000 000.

Roex, A.P., Späth, A. and Zartman, R.E., 2001. Lithospheric thickness beneath the southern Kenya Rift: implications from basalt geochemistry. Contributions to Mineralogy and Petrology, vol. 142, no. 1, p. 89-106.

Rogers, N. (2015). The composition and origin of magmas. The Encyclopedia of Volcanoes, Elsevier, p. 93-112.

Roots, C.F., 1988. Cambro-Ordovician Volcanic Rocks in Eastern Dawson Map-Area, Ogilvie Mountains, Yukon. In: Yukon Exploration and Geology 1988, J.G. Abbott (ed.), Exploration and Geological Services Division, Yukon Region, Indian and Northern Affairs Canada, vol. 2, 7 p.

Schmitz, M.D. and Schoene, B., 2007. Derivation of isotope ratios, errors and error correlations for U-Pb geochronology using 205Pb-235U-(233U)-spiked isotope dilution thermal ionization mass spectrometric data. Geochemistry, Geophysics, Geosystems (G3), vol. 8, Q08006, https://doi.org/10.1029/2006GC001492.

Shinjo, R., Chung, S.L., Kato, Y. and Kimura, M., 1999. Geochemical and Sr-Nd isotopic characteristics of volcanic rocks from the Okinawa Trough and Ryukyu Arc: Implications for the evolution of a young, intracontinental back arc basin. Journal of Geophysical Research: Solid Earth, vol. 104, no. B5, p. 10591-10608.

Sláma, J., Košler, J, Condon, D.J., Crowley, J.L., Gerdes, A., Hanchar, J.M., Horstwood, M.S.A., Morris, G.A., Nasdala, L., Norberg, N., Schaltegger, U., Schoene, B. Tubrett, M.N. and Whitehouse, M.J., 2008. Plešovice zircon — A new natural reference material for U–Pb and Hf isotopic microanalysis. Chemical Geology, vol. 249, p. 1-35.

Spitz, G. and Darling, R., 1978. Major and minor element lithogeochemical anomalies surrounding the Louvem copper deposit, Val d'Or, Quebec. Canadian Journal of Earth Sciences, vol. 15,no. 7, p. 1161-1169.

Strauss, J.V., Roots, C.F., MacDonald, F.A., Halverson, G.P., Eyster, A. and Colpron, M., 2014. Geological map of the Coal Creek Inlier, Ogilvie Mountains (NTS116B/10-15 and 116C/9,16). Yukon Geological Survey Open File 2014-15, 1:100 000 scale.

Sun, S.S.and McDonough, W.F., 1989. Chemical and isotopic systematics of oceanic basalts: implications for mantle composition and processes. In: Magmatism in ocean basins, A.D. Saunders and M.J. Norry (eds.), Geological Society of London, Special Publication 42, p. 313-345.

Tanaka, T., Togashi, S., Kamioka, H., Amakawa, H., Kagami, H., Hamamoto, T., Yuhara, M., Orihashi, Y., Yoneda, S. and Shimizu, H., 2000. JNdi-1: a neodymium isotopic reference in consistency with LaJolla neodymium. Chemical Geology, vol. 168, no. 3-4, p. 279-281.

Thompson, R., Roots, C. and Mustard, P., 1994. Geology of Dawson map area (116B, C, northeast of Tintina Trench). Geological Survey of Canada, Open File 2849.

van Staal, C.R., Winchester, J.A. and Bédard, J.H., 1991. Geochemical variations in Middle Ordovician volcanic rocks of the northern Miramichi Highlands and their tectonic significance. Canadian Journal of Earth Sciences, vol. 28, p. 1031-1049.

Watson, E.B., Wark, D.A. and Thomas, J.B., 2006. Crystallization thermometers for zircon and rutile. Contributions to Mineralogy and Petrology, vol. 151, p. 413-433.

Weis, D., Kieffer, B., Hanano, D., Nobre Silva, I., Barling, J., Pretorius, W., Maerschalk, C. and Mattielli, N., 2007. Hf isotope compositions of US Geological Survey reference materials. Geochemistry, Geophysics, Geosystems, vol. 8, no. 6, 15 p.

Weis, D., Kieffer, B., Maerschalk, C., Barling, J., De Jong, J., Williams, G.A., Hanano, D., Pretorius, W., Mattielli, N. and Scoates, J.S., 2006. High-precision isotopic characterization of USGS reference materials by TIMS and MC-ICP-MS. Geochemistry, Geophysics, Geosystems (G^3), vol. 7, no. 8, 30 p.

Whitford, D.J., McPherson, W.P. and Wallace, D.B., 1989. Geochemistry of the host rocks of the volcanogenic massive sulfide deposit at Que River, Tasmania. Economic Geology, vol. 84, no. 1, p. 1-21.

Wiedenbeck, M.A.P.C., Alle, P., Corfu, F.Y., Griffin, W.L., Meier, M., Oberli, F.V. and Spiegel, W., 1995. Three natural zircon standards for U-Th-Pb, Lu-Hf, trace element and REE analyses. Geostandards newsletter, vol. 19(1), p. 1-23.

Yonkee, W., Dehler, C., Link, P.K., Balgord, E., Keeley, J.A., Hayes, D., Wells, M., Fanning, C. and Johnston, S., 2014. Tectono-stratigraphic framework of Neoproterozoic to Cambrian strata, west-central US: Protracted rifting, glaciation, and evolution of the North American Cordilleran margin. Earth-Science Reviews, vol. 136, p. 59-95.

Yukon Geological Survey, 2024. Yukon Digital Bedrock Geology. Yukon Geological Survey, http://datatest.geology.gov.yk.ca/Compilation/3 [accessed: April 2024].

Appendix A

Appendix B

Appendix C

Yukon Geological Survey
Energy, Mines and Resources
Government of Yukon